Fibre Laser Array for Power Scaling of a Line-Beam Source

PETER RENTSCHLER

Master of Science Thesis
Department of Applied Physics
KTH – Royal Institute of Technology
Stockholm, Sweden 2010

Fibre Laser Array for Power Scaling of a Line-Beam Source

Laser Physics
Department of Applied Physics
KTH – Royal Institute of Technology
106 91 Stockholm
Sweden

TRITA-FYS 2010:55
ISSN 0280-316X
ISRN KTH/FYS/--10:55--SE

Printed by Universitetsservice US AB, Stockholm 2010

Abstract

In this thesis, a line-like laser beam profile is generated by parallel stacking of several fibre lasers, which provides a convenient way to scale the total output power of the line source.

It is shown, using a setup with three parallel Yb-doped fibre lasers operating at 1030 nm, that linear power scaling can be achieved, and a total output power of approximately 9 W is obtained. The output is made linearly polarized by use of polarization maintaining fibres and an intra-cavity polarizer, which yielded polarization extinction ratios between 13 and 23 dB. A spectrally narrowband output of below 0.1 nm (23 GHz) was obtained using a volume Bragg grating, such that nonlinear frequency conversion to the visible and the ultraviolet could be performed.

Evaluation of the array beam profile shows good agreement with a simulation of the output and a nearly top-hat intensity distribution is obtained. This shows that the fibre array is a promising approach to scale the power of line-shaped laser sources.

Contents

Acknowledgements

This thesis has been carried out in the Laser physics group of the Department of Applied Physics at KTH, the Royal Institute of Technology in Stockholm, Sweden. The reason that this final stroke of my master studies has become a successful one, is thanks to many people whom I would like to thank here.

First and most of all, thanks Björn! Björn Jacobsson was my supervisor and due to his guidance and support – with still enough freedom to actualize my own ideas and thoughts – this thesis has become an extremely valuable experience for me.

Also, many thanks to my examiner, Fredrik Laurell. He accepted me as a diploma worker in his group and therefore, gave me the opportunity to write my thesis in this great environment.

My gratitude also goes to all other members of the group and the department, for I have bullied some of them quite a bit over the last few months.

Of course, thanks to all new and old friends with whom I could either have lively discussions about "Lazers", or simply one or two drinks to get some distance every now and then, which was equally important.

And last but not least, I would like to thank my family. Without their financial and moral support I could not have spent two great years of my life studying in Sweden.

List of abbreviations and symbols

The following abbreviations and symbols for physical quantities are used throughout the thesis.

λ_0	Vacuum wavelength of light
θ_a	Acceptance angle of a fibre
a	Fibre core radius
BPP	Beam parameter product
c	Speed of light in vacuum
FBG	Fibre Bragg grating
FWHM	Full width at half maximum
I	Intensity
IR	Infrared
n	Refractive index
NA	Numerical aperture
P	Power
r	Radial coordinate
SFG	Sum frequency generation
SHG	Second harmonic generation
SLM	Spatial light modulator
UV	Ultraviolet
V-number	Fibre parameter or normalized optical frequency
VBG	Volume Bragg grating
w	Mode field radius

Chapter 1

Introduction

Lasers are one of the most versatile lightsources nowadays. They can combine beam properties such as monochromaticity, coherence and high brightness into beams with several megawatts of output power. Laser beams are most commonly circular in cross-section, however, there is a variety of applications which require alternative beam profiles, for instance rectangular profiles with uniform intensity, as used for material processing [1, 2], a doughnut profile for stimulated emission depletion (STED) microscopy [3] or a line profile, to name only a few.

In particular, a line beam has a number of interesting applications, such as for displays [4, 5] or laser writing [6]. In both applications, information has to be brought to a designated surface area.

Covering an area with one beam is usually performed with active deflection optics. For pixel-by-pixel scanning with a circular spot as shown in Fig. 1.1(a), these mirror modules are rather complex, since they need two rotational degrees of freedom to deflect the beam in the x- and the y-direction. This can for instance be achieved by piezo-driven tilt mirrors. Using a line-beam, the complexity is shifted from the mirror element to the light source, as shown in Fig. 1.1(b). For instance, if the line is modulated (i. e. information is imposed) along its long dimension with a spatial light modulator (SLM), it is sufficient to deflect the beam along the short line dimension, e. g. with a simple rotating polygon mirror.

The most important advantage of the line over the pixel-by-pixel approach, is the scanning speed. In writing applications, a higher speed reduces the scanning time and increases the throughput. For displays on the other hand, it will determine the maximum size and resolution of the projected image.

There is, however, another constraint which is related to speed, namely the deposited energy or intensity. This quantity is determined by a particular application. If, for instance, laser writing is used to directly expose a photoresist for optical lithography, the minimum exposure time will be determined by the intensity which is needed for the dissolved polymers to undergo a structural change,

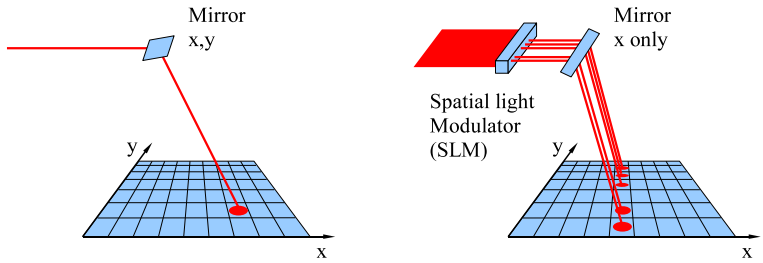

(a) Pixel-by-pixel scanning (b) Line scanning

Figure 1.1: Pixel-by-pixel vs. line-wise scanning.

such as hardening, in case of a negative photoresist. The minimum intensity for a very sensitive resist might be as low as $10 - 100$ mW/cm^2 [7], but can be several orders of magnitude higher for other applications. The system has to be capable of delivering this amount of energy, otherwise, it will limit the maximum scanning speed.

The idea which is investigated in this thesis is to scale the output power of a line beam, by stacking several fibre lasers along the direction with relaxed constraints on beam quality, namely the long line dimension. Fibre lasers are particularly suitable for this approach, since they can deliver output powers of over 100 W, while still providing a high beam quality [8]. Moreover, due to the small fibre diameter of only a few hundred microns, they can be stacked very closely, thus giving the potential for very high power scaling.

For display and laser writing applications, it is required that the wavelength of the output can be changed, namely into visible light (green) for diplays and UV light for laser writing in order to obtain a small minimal feature size. To achieve frequency conversion by a nonlinear process, a spectrally narrow and linearly polarized output is required, both of which can be delivered by fibre lasers [9]. The near infrared spectrum at wavelengths of around 1 µm is a particularly convenient region, since frequency doubling and tripling directly yields green and UV light, respectively.

The design goal was therefore to build an array of three parallel, Yb-doped fibre lasers with a total output power of approximately 10 W, as well as a linearly polarized and spectrally narrow output, operating at 1030 nm.

1.1 Design Approaches

The individual fibre lasers can be built in various cavity configurations. The following two were considered for this thesis:

The first option is an all-fibre design as shown in Fig 1.2. It consists of a fibre-coupled pump source which is spliced to a highly reflective fibre Bragg grating (FBG). The pump light is transmitted through the cladding of the FBG and is coupled into the gain fibre which is spliced to the opposite end of the FBG. The output coupler is another FBG, spliced on the other end of the gain fibre, however with a lower reflectivity (e. g. 15 %).

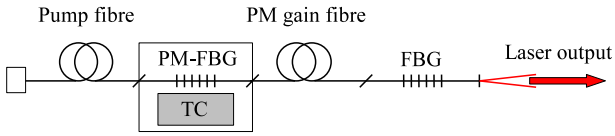

Figure 1.2: All-fibre cavity design.

The highly reflective FBG is written into a polarization maintaining (PM) fibre, hence, it will exhibit two reflection peaks, due to the fibre's birefringence (each reflection peak corresponds to one polarization direction of the light, for more details on PM-fibres, see section 2.1). The reflection peaks can be shifted by temperature controlling (TC) the grating. If the temperature is tuned such that one of the reflection peaks of the PM-FBG coincides with the single reflection peak of the out-coupling grating, lasing will occur on that particular wavelength and with that particular polarization direction.

Using similar setups, output powers of up to hundreds of watts have been demonstrated, which also meet the requirements of the array in terms of spectral width and polarization [10–13]. The all-fibre approach allows for very robust designs with only a few control parameters, since only very few external optics are needed. However, this design lacks of flexibility and the access to components is limited. Expanding the setup and replacing components is problematic, since the spliced fibre joints are permanent.

The second approach utilized free-space coupling of the pump and output beam, as illustrated in Fig. 1.3.

Coupling of the pump beam into the gain fibre is achieved with lenses. On the opposite end of the gain fibre, the collimated output beam is aimed on the highly reflective cavity mirror. Fresnel reflections at the cleaved fibre end-face on the pump side act as the output coupler. The laser output is separated from the pump beam using a dichroic mirror.

This approach has the advantage of easy access to components and a high flexibility. The setup can easily be expanded e. g. with polarizers, wave-plates or filters and replacing broken components is straightforward. On the other hand, due to the increased number of optical elements, the alignment of the laser will be more challenging.

Due to the higher design-freedom and good availability of components, the free-space approach was chosen for building the single fibre lasers in this thesis.

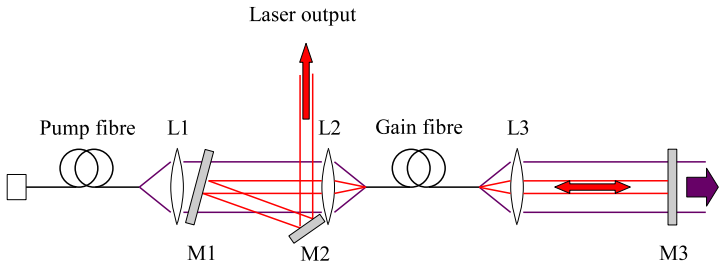

Figure 1.3: Fibre laser design utilizing free-space coupling.

1.2 Outline of the Thesis

The thesis is structured as follows: In the second chapter, a short introduction to the basic physics of fibre lasers is given. It is followed by a simulation of the output from an array of parallel fibre lasers. A description of the pump mount and a characterization of the used pump lasers is presented in chapter 4. Chapters 5 to 7 describe experiments with single fibre lasers, where in each chapter, a new feature is added to achieve the desired output. Chapter 8 describes the setup and the performance of the fibre laser array. Experiments on nonlinear frequency conversion are presented in chapter 9 and finally, in chapter 10, the results of the thesis are summarized and conclusions are drawn.

Chapter 2

Basic Physics

The following chapter gives a very brief introduction to the working principles and theory of fibres and lasers. It will cover only the topics which are needed for a good understanding of this thesis, however, it makes no claim to be complete. Further reading can be done in any standard textbook, e. g. [14–16].

2.1 Optical Fibres

Optical fibres guide light based on the principle of total internal reflection. They are commonly made from silica glass and the simplest type consist only of a fibre core with refractive index n_1 which is surrounded by a cladding with refractive index n_2 (Fig. 2.1). For $n_1 > n_2$, the light is confined to the fibre core. Since the

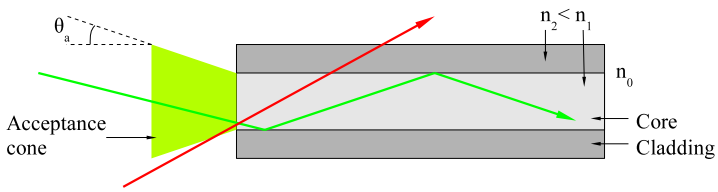

Figure 2.1: Schematic drawing of a step index fibre with $n_1 > n_2$. Light is coupled into the fibre if it impinges on the front surface from within the acceptance cone.

refractive index profile in radial direction only takes two values, they are usually referred to as step-index fibres. Due to their low loss of only a few dB/km or less, fibres are very suitable for delivering light to places which are otherwise difficult to reach or even inaccessible.

Numerical Aperture

An important characteristic of optical waveguides is their numerical aperture (NA). In accordance with classical optics, the NA is defined as the sine of half the acceptance angle of the fibre, θ_a, multiplied by the refractive index of the surrounding medium, n_0. For step-index fibres, the NA can be derived directly from the index difference between core and cladding and is given by:

$$\mathrm{NA} = n_0 \sin(\theta_a) = \sqrt{n_1^2 - n_2^2} \tag{2.1}$$

When light is coupled into a fibre with a lens, the convergence angle of the focussed beam and the focal spot size are dependent. The numerical aperture and core size therefore determine e. g. how efficient light can be launched into a fibre. Moreover, they will determine how well the light is confined in the core; hence, it will affect the mode field size and thus the divergence angle of the emerging beam.

Transverse Electromagnetic Modes and V-Number

Depending on the core/cladding geometry and the glass composition, the field distribution $u(r)$ within the fibre will look differently. It can be found by solving the wave equation for a cylindrical waveguide. The solutions are usually referred to as the transverse electromagnetic modes of the fibre [17]. For a step-index fibre with core radius a, the field at radial coordinate r is given by:

$$u(r) = \begin{cases} J_l(k_T r), & r < a \\ K_l(\gamma r), & r > a \end{cases} \tag{2.2}$$

J_l and K_l are the Bessel functions of the first and second kind, respectively, both of order l. The parameters $k_T^2 = k_1^2 - \beta^2$ and $\gamma^2 = \beta^2 - k_2^2$ depend on the wavenumber $k_i = 2\pi n_i/\lambda_0$ and the effective propagation constant β of the wave. For a guided wave, the propagation constant can take values of $k_1 > \beta > k_2$ and is found by graphically solving the characteristic equation

$$X \frac{J_{l\pm1}(X)}{J_l(X)} = \pm Y \frac{K_{l\pm1}(Y)}{K_l(Y)}, \tag{2.3}$$

such that $u(r)$ is continuous and has a continuous derivative at $r = a$. The quantities $X = k_T a$ and $Y = \gamma a$ are normalized coordinates.

A very useful quantity to estimate the number of transverse modes is the V-number. It is defined as

$$V = \sqrt{X^2 + Y^2} = \frac{2\pi a}{\lambda_0}\mathrm{NA} \tag{2.4}$$

and can be interpreted as a normalized optical coordinate.

In general, a superposition of many transverse modes exist in a fibre. The total intensity distribution $I(r, \phi)$ of a superposition is proportional to

$$I(r, \phi) \propto u_{l,m}^2(r) \cos^2(l\phi), \tag{2.5}$$

where the the integers l and m are found by solving Eq. 2.3 and ϕ is the rotational coordinate around the fibre's symmetry axis.

For values of V below 2.405 the fibre supports only the fundamental mode ($l = m = 0$). This is often desired, since multimode operation increases dispersion and decreases the beam quality. Furthermore, the intensity distribution of the fundamental mode can to a very good approximation be described by a Gaussian function.

Mode Field Size

The V-number also allows to estimate the mode field radius w for a given fibre during single-mode operation [18]. It is approximately given by:

$$w \approx a \left(0.65 + \frac{1.619}{V^{3/2}} + \frac{2.879}{V^6}\right) \tag{2.6}$$

The equation is accurate to within 1 % for V-numbers up to 2.5. For higher values, it only applies to the size of the fundamental mode.

Polarization Maintaining Fibres

In general, fibres are not perfectly isotropic, but they exhibit random stress fluctuations. The stress fluctuations induce locally varying birefringence, so that linearly polarized light will change to circularly polarized light as it propagates along the fibre. There are, however, fibres which can maintain the polarization direction of the incoupled light, so-called polarization maintaining (PM) fibres.

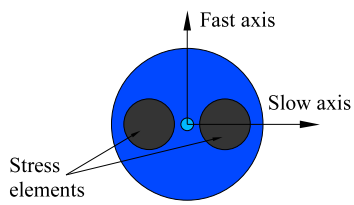

Figure 2.2: The stress elements in a PM fibre create birefringence so that polarized light which is launched into the fibre along one of the birefringent axis maintains its polarization direction.

In a PM fibre, glass rods of different thermal expansion coefficient than the bulk material are inserted diametrically opposed around the fibre core, as can be seen

in Fig. 2.2. When the fibre is drawn and cooled down, the rods exert high stress on the fibre core along one distinct direction, which is then the dominant stress contribution in the fibre. Hence, two designated, perpendicular axis of birefringence are established. The axes with higher refractive index is referred to as the slow axis of the fibre.

When light is coupled into the fibre along either the slow or the fast axis, it maintains its polarization direction and does not couple into other polarization modes.

2.2 Lasers

All lasers consist of a active gain medium which is placed in a resonant cavity. As shown in Fig. 2.3, the resonant cavity usually consists of one highly reflective mirror and one output coupler with lower reflectivity. With each passing through the gain medium, the light is amplified and at every reflection at the output coupler a fraction of the light leaves the cavity. This fraction of the light constitutes the laser beam. The active medium is made from a host material, e. g. glass or crystals which are doped with an active material. These are usually ions from rare-earth elements such as Yb, Er or Nd. The seed for the amplification process is spontaneous emission, which is always present if the active medium is pumped.

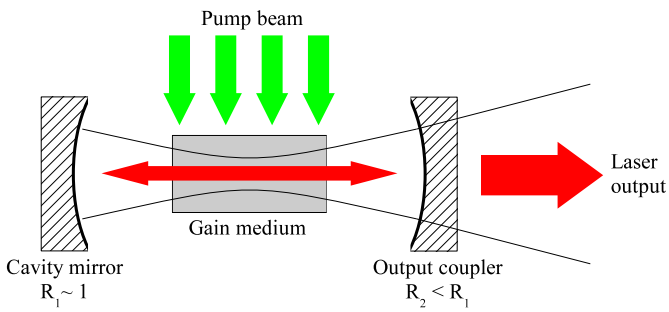

Figure 2.3: Principal scheme of a laser. Light is contained in the laser cavity and is amplified at each passage through the gain medium. At each reflection on the output coupler, a fraction of the light leaves the cavity and constitutes the laser beam.

Ytterbium

The active material which was used in this thesis was the Ytterbium ion in the trivalent form, Yb^{3+}. It has properties which make it particularly useful for high-power applications, such as its simple energy level diagram and a very low quantum defect. The energy level diagram is shown in Fig. 2.4. It consists of two manifolds;

the ground manifold ${}^2F_{7/2}$ with 4 Stark levels and the excited manifold ${}^2F_{5/2}$ with 3 Stark levels [19].

The upper laser level can be reached by pumping with near infrared light, e. g. the transition with maximum absorption, from the lowest Stark level of the ground manifold to the lowest Stark level of the excited manifold, corresponds to a wavelength of 975 nm, a wavelength at which high power pump sources are easily available.

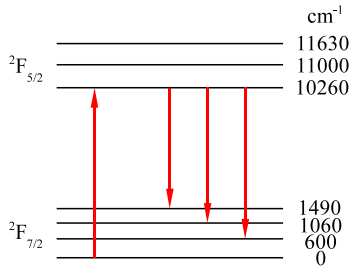

Figure 2.4: Energy level diagram of the Yb^{3+}-ion.

Commonly used laser transitions are from the lowest Stark level of the upper manifold to several of the upper Stark levels of the ground manifold. Together with efficient phonon broadening, this results in a broad emission spectrum that permits laser operation from $1 - 1.2$ µm, and also allows for short pulse generation.

A particularly interesting wavelength for frequency conversion is at around 1 µm, since frequency doubling and tripling directly yields green and ultraviolet light.

Given the high power capability and the convenient transitions in the near-infrared spectral region, ytterbium was chosen as the gain material for the experiments in this thesis.

2.3 Fibre Lasers

Fibre lasers combine the properties of both aforementioned components. In such lasers, the doped core of a fibre constitutes the active medium of the laser. The active fibre can be several tens of metres long, giving rise to a very high gain. Furthermore, due to the high ratio of area to volume, thermal effects in high-power systems are reduced. Fibre lasers are often optically pumped, utilizing a double-clad (DC) structured fibre as shown in fig. 2.5. In such fibres, the core is surrounded by an inner cladding with lower refractive index than the core which is in turn surrounded by an outer cladding with even lower refractive index.

The inner cladding has a considerably larger cross-section and NA than the core, such that pump light with relatively poor beam quality can still be coupled efficiently into the fibre. The pump light is confined to the inner cladding and gradually absorbed in the core. Laser operation however, will occur in the fibre core

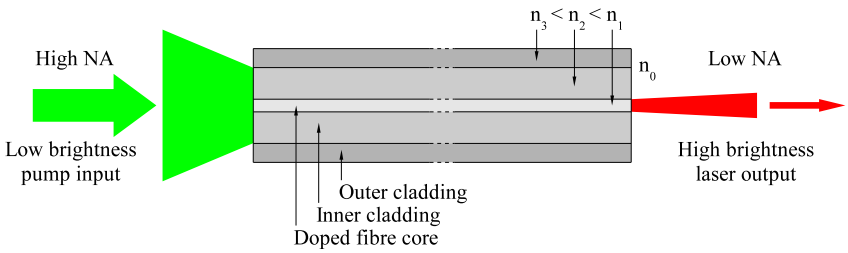

Figure 2.5: Schematic drawing of a double-clad (DC) fibre. With additional reflective elements on the fibre end faces, a DC-fibre can be used to convert pump light with poor beam quality into a laser beam with high brightness and M^2-factors close to 1.

only. The core has a low NA, typically below 0.1, giving rise to a high-brightness output. Therefore, fibre lasers can convert the beam from a low-brightness pump source into laser light of very high beam quality.

Very robust lasers can be built in all-fibre configurations, using e. g. fibre Bragg gratings for feedback. This and their capability of approaching a diffraction limited beam quality – even at kilowatts of output power – make fibre lasers particularly suitable for a wide range of applications.

2.4 Gaussian Beams

The intensity distribution of many laser beams can be described with a Gaussian function. Such a beam profile can be described by the beam's peak intensity I_0 and the beam radius from the optical axes $w(z)$, at which the intensity has dropped to $1/e^2$ of its maximum value. The intensity after propagation over a distance z is given by

$$I(r,z) = I_0 \exp\left(\frac{-2r^2}{w(z)^2}\right), \tag{2.7}$$

where r is the (orthogonal) distance from to the optical axis at which the beam has intensity $I(r,z)$.

Moreover, as a result of diffraction, a Gaussian beam will diverge as it propagates. The beam radius as a function of propagation distance is given by

$$w(z) = w_0\sqrt{1+\left(\frac{z}{z_\mathrm{R}}\right)^2}, \tag{2.8}$$

where $w_0 = w(z{=}0)$ is the beam waist radius and z_R is the distance from the waist after which the beam radius has increased by a factor of $\sqrt{2}$ (i. e. where the effective beam area has doubled). This distance is referred to as the Rayleigh range and can

be calculated from the laser wavelength λ and the beam waist according to:

$$z_{\mathrm{R}} = \frac{\pi w_0^2}{\lambda} \tag{2.9}$$

Two times the Rayleigh range is referred to as the confocal parameter b:

$$b = 2z_{\mathrm{R}} \tag{2.10}$$

In the far field where $z \gg z_{\mathrm{R}}$, the divergence angle from the optical axis, θ, can easily be calculated from Eqs. 2.8 and 2.9. Differentiation of Eq. 2.8 with respect to z yields:

$$\theta = \frac{\lambda}{\pi w_0} \tag{2.11}$$

Beam Parameter Product and M^2-Factor

A diffraction limited Gaussian beam is special in a sense as it minimizes the product of its beam radius at the beam waist, w_0, and its far-field half divergence angle, θ. This quantity is referred to as the beam parameter product (BPP) and for a diffraction limited Gaussian beam it reduces to:

$$\mathrm{BPP}_{\mathrm{G}} = w_{0,\mathrm{G}}\theta_{\mathrm{G}} = \frac{\lambda}{\pi} \tag{2.12}$$

where the subscript "G" denotes quantities of a diffraction limited Gaussian beam.

A very important quality measure of laser beam is therefore defined as the ratio of its BPP and the BPP of a Gaussian beam. It is referred to as the beam's M^2-factor and is 1 only for a diffraction limited Gaussian beam:

$$M^2 = \frac{\mathrm{BPP}}{\mathrm{BPP}_{\mathrm{G}}} \tag{2.13}$$

Using the M^2-factor, one can therefore relate the two parameters of a beam, θ and w_0, according to:

$$\theta = M^2 \frac{\lambda}{\pi w_0} \tag{2.14}$$

One consequence of this relation is, that if a given light source is focussed to a point, the spot diameter in the focal plane will increase linearly with the M^2-value of the source.

Chapter 3

Array Simulation

To understand the behaviour of the system, the output beam of an array of fibre lasers was simulated. In the setup, the fibres are mounted in parallel next to each other at close distance. As is well-known, the diameter of a Gaussian beam increases as the beam propagates. Hence, the individual beams of the array will eventually merge and after some distance, when the beam diameter is much larger than the fibre separation, the beams will no longer be distinguishable. The simulation allows to find the distance after which the beams have merged to the desired intensity distribution.

The wavelength of the light and the V-number of the fibres which were used in the experiments, were assumed to be 1030 nm and 2.44, respectively. Using the V-number and Eq. 2.6, the diameter of the mode field where the intensity has dropped to e^{-2} of its maximum value was found to be approximately 11 µm. The beam waist diameter of the emitted Gaussian beam was assumed to have the same size as the mode field within the fibre.

The simulation gives the output from any number of fibres with equal separation distance. For some applications it is beneficial to deposit as much energy on a given spot as possible. Therefore, the fibres are stacked as closely as possible. The minimum distance between the fibre cores is determined by the diameter of the fibre cladding, namely 125 µm.

Fig. 3.1 shows the intensity distributions for five fibre lasers at a number of different propagation distances. The left column shows the intensity distribution in the plane perpendicular to the propagation. The right column shows the cross-section through the line of maximum intensity. Note that the images in the left column are scaled with the spot diameter $2w$ of a single fibre laser as given by Eq. 2.8. The scaling was such that the vertical size of the image corresponds to the diameter at which the intensity has dropped to e^{-2} of the peak value at that particular propagation distance.

A different visualization of how the beams merge can be seen in Fig. 3.2. It shows

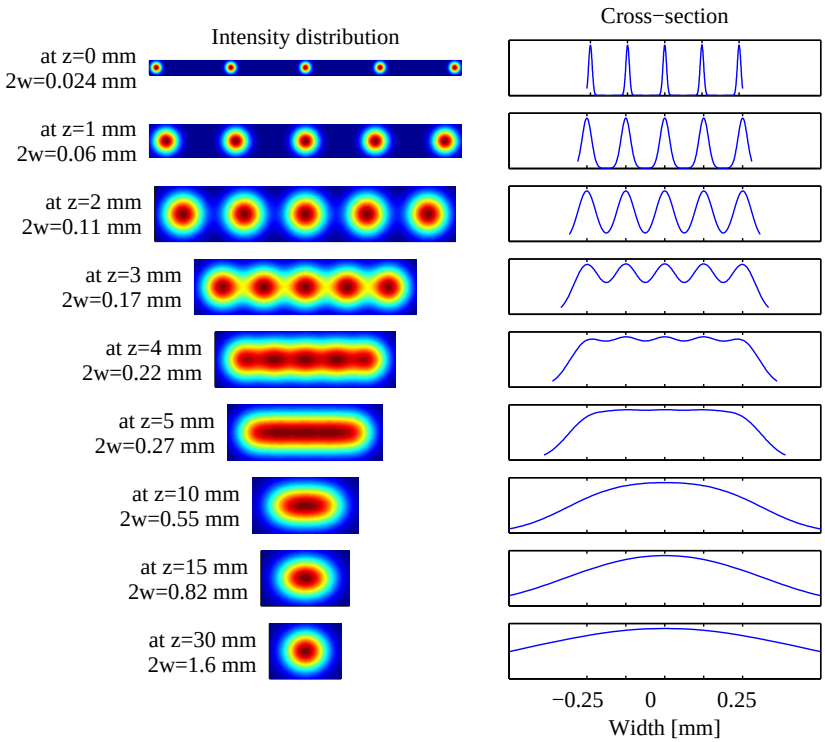

Figure 3.1: Simulated output from an array of five fibre lasers. The left column shows the intensity distribution in a plane perpendicular to the propagation direction. The image height is scaled with the spot diameter $2w$. The right column shows the cross-section through the line of maximum intensity of all fibres.

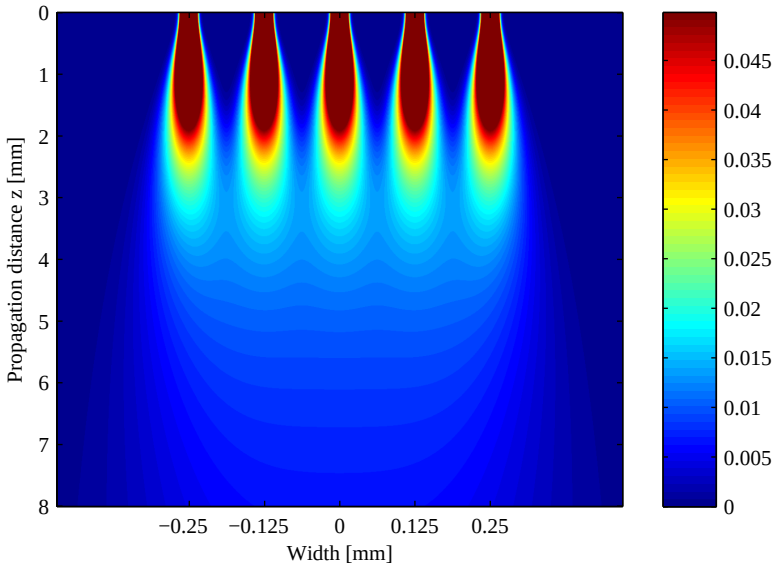

Figure 3.2: Intensity distribution in the fibre plane. The fibre separation is 125 µm. Note that the intensity is truncated such that values above $0.05\, I_{\max}$ are cut off.

the cross-section through the centre of the beam as in Fig. 3.1, but continuously for a range in propagation direction from 0 to 8 mm. The maximum intensity decreases with propagation distance. Furthermore, the drop in intensity along the lateral direction is more distinct close to the fibre ends. In the far-field, the intensity decreases only gradually as the lateral distance from the fibres increases.

For many applications, the ideal intensity profile is a top-hat distribution. A top-hat has no spatial modulation in the region where the intensity is "high", so that e. g. the energy in a writing application can evenly be deposited. Furthermore, it shows no gradual decrease in intensity in the lateral direction, only a sharp transition from the "high"- to the "low"-intensity region.

To quantify how well the intensity distribution resembles a top-hat profile, a fill-factor Γ was defined. It is given by the power of the output profile where a certain intensity-threshold is exceeded, divided by the total output power. In Fig. 3.3, this fraction is enclosed by the green top-hat function, and has a value of $\Gamma = 82\,\%$ (at $z = 4$ mm). The threshold I_{th} will depend on the application in particular and is in this example defined as $I_{\text{th}} = 0.9 I_{\max}$. As a rule of thumb, it can be approximated that at each side of the total intensity distribution, one half of the power from a

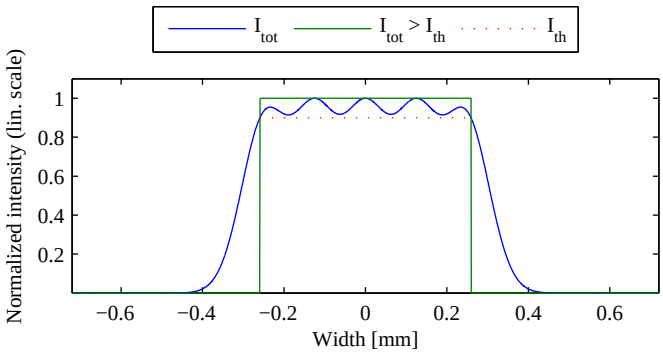

Figure 3.3: The fill-factor Γ is a measure of how well the output profile resembles an ideal top-hat function. It is given by the ratio of powers in the intensity profile with $I > I_{\mathrm{th}}$ and the total power of the beam. The threshold is this example is arbitrarily defined as $0.9 I_{\mathrm{max}}$. More quality measures of the beam are the intensity modulation inside the hat and the corresponding standard deviation. (Plot at $z = 4$ mm)

single laser is lost. Hence the fill-factor is approximately given by:

$$\Gamma \approx \frac{n_{\mathrm{fibres}} - 1}{n_{\mathrm{fibres}}}, \tag{3.1}$$

where n_{fibres} is the number of fibres in the array. For five fibres this yields $\Gamma = 80\,\%$ which coincides well with the exact value above. Note that this approximation is only valid if the fibre separation is of the same order of magnitude as the beam radius $w(z)$ and the threshold is not too low.

Another quality-measure of the array is the intensity modulation of the profile which is contained inside the top-hat. It is defined as the ratio of the amplitude of the modulation and the mean intensity within the top-hat $\bar{I}_{\mathrm{hat}}$ (see also Fig. 5.7). The modulation has to be sufficiently low, so that the intensity within the top-hat does not drop below the threshold value. One can therefore define the critical maximum modulation M_{crit} approximately as

$$M_{\mathrm{crit}} \approx 1 - \frac{I_{\mathrm{th}}}{\bar{I}_{\mathrm{hat}}}. \tag{3.2}$$

In the example from Fig. 3.1, the region with good modulation lies at around $z = 4$ mm. At this point, the modulation is 5 %, which is below the critical value $M_{\mathrm{crit}} = 5.4\,\%$.

Another measure of the beam, which is related to the modulation, is the standard deviation σ of the intensity distribution inside the top-hat. Its variation with z is shown in Fig. 3.4. It can be seen in Fig. 3.4, that there is a distinct minimum

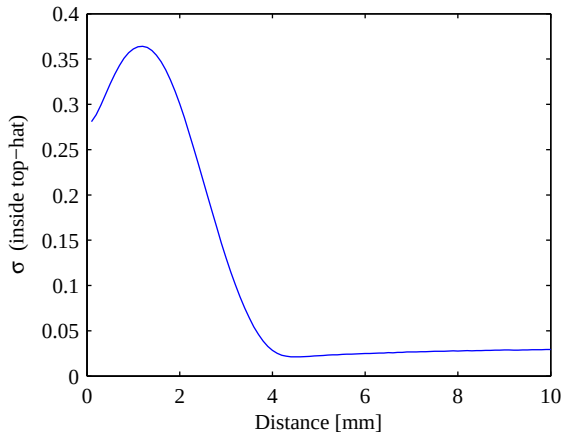

Figure 3.4: Standard deviation σ of the intensity profile within the top-hat vs. propagation distance.

at approximately $z = 4.5$ mm. This can e. g. be utilized to find the position of the "best" beam, which will be a trade-off between the fill-factor and the standard deviation. The importance of each parameter must be chosen according to the application and will in particular depend on the number of fibres.

If the fibre pitch is increased, then the region of interest moves further away. The same effect is obtained if the fibre NA is decreased since the divergence angle reduces accordingly. There is a linear dependence between fibre pitch, fibre NA and the distance to the region of interest.

Note that if intermediate optics are used for imaging of the fibre ends, both the fibre pitch and the divergence angle in the image plane change. Therefore, if the fibre ends are imaged with a magnification of $m = 2$, the region of interest will be four times further away.

Chapter 4

Pump Laser

To operate a laser, energy has to be transferred to its active medium. This process is referred to as pumping. For the fibre lasers which are used in this thesis, optical energy is used to pump the gain fibres. The pump sources are three fibre-coupled single emitter laser diodes which radiate at approximately 975 nm (Lumics LU975T100). The diodes have serial numbers HL110275, HL110279 and HL112105, but will for convenience from here on only be labelled LD1, LD2 and LD3. The light is delivered with a standard step-index fibre with core and cladding diameter of 105 and 125 nm, respectively. The NA of the core is 0.22.

The output characteristics of semiconductor lasers are sensitive to the driving current and the temperature at which they are operated. Therefore, a mount was built on which the diodes could be temperature controlled and conveniently connected to the driver electronics. Since at a later stage of this thesis, three fibre lasers are to be operated simultaneously, the mount is designed such that it can hold three pump diodes. This allows that all pumps can be controlled with a single driver. The device is illustrated in Fig. 4.1.

4.1 Diode Mount

The heat sink consists of a 1 cm thick copper plate as a heat reservoir on which the diodes are mounted, three 3-by-3 cm Peltier elements (Melcor CP10-127-05-L1-W4.5) to electronically control the temperature of the reservoir and a fan unit (Elfa 75-591-56) to cool the hot side of the Peltier elements. The Peltier elements are connected in parallel and are driven by a temperature controller from Marlow Industries (model SE5020). The temperature sensor is a thermistor with negative temperature coefficient (NTC) and $R_0 = 10\,\mathrm{k}\Omega$ at 25 °C. It is placed in a notch close to the surface of the copper plate between two laser diodes (see Fig. 4.2). The wiring can be seen in Fig. 4.1. Connectors ① and ② are for the positive and negative ports of the current source of the temperature controller. The NTC uses

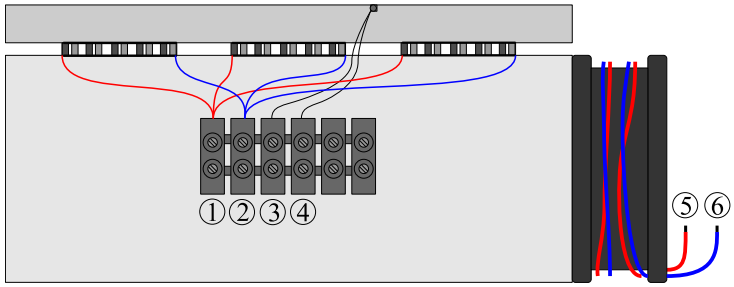

Figure 4.1: Heat sink with wiring of the Peltier elements (① and ②), temperature sensor (③ and ④) and fan (⑤ and ⑥).

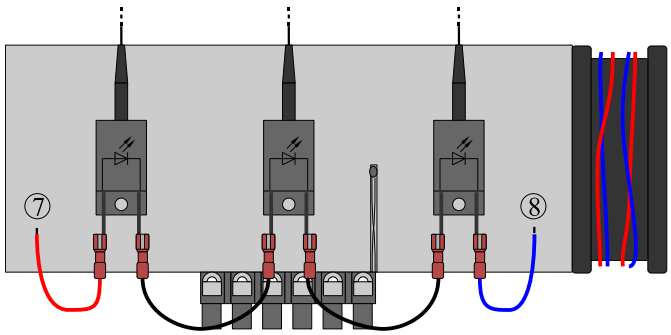

Figure 4.2: Heat sink with laser diodes. The driver is connected to the diodes via ports ⑦ (+) and ⑧ (–).

ports ③ and ④. This device is bidirectional, so the polarity can be arbitrary. ⑤ and ⑥ are connected to the positive and negative poles of a standard 12 V power supply. A luster terminal is used which enables easy changes of the wiring if needed.

The laser diodes are clamped onto the copper plate above each Peltier element as can be seen in Figs. 4.1 and 4.2. The wiring is done with pin-and-socket connectors in order to easily bypass one or two diodes if they are not needed. The current supply is provided by a driver from Opto Power Corporation (model OPC-PS 4005). It can provide a current of up to 30 A. This ensures that it can supply the voltage to drive a series of three 10 A laser diodes, as used in this setup. Connector ⑦ is for the positive port of the power supply, whereas ⑧ is for the negative one. For experiments with only one diode, wires are used to short-circuit the unused diodes and the active laser is directly connected to the driver.

4.2 Pump Laser Characteristics

The performance of the fibre lasers will change with the incident pump power. Since the control variable is the current through the diodes, a measurement has been conducted to relate these two quantities. The output characteristics can be see in Fig. 4.3. The graph shows that the behaviour is linear only for moderate

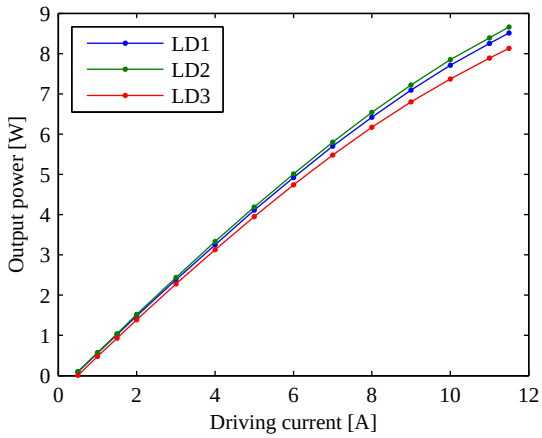

Figure 4.3: Output power of the pump diodes vs. driving current.

driving currents up to approximately 6 A. Beyond this point the slope of the curve decreases. The maximum output power is around 8.5 W.

Thermal effects within the band gap of the semiconductor lead to a drift in output wavelength with temperature. This can either be caused by the temperature of the heat sink or the driving current. Since the absorption cross-section of the fibre strongly depends on wavelength, it is important to know about the output spectrum for a given temperature and driving current. The spectra of the diodes were measured with an optical spectrum analyzer (OSA) from Yokogawa (model AQ-6315A) under different operating conditions. The spectra close to maximum driving current are depicted in Fig. 4.4. The spectral resolution was 0.1 nm. The vertical dotted lines in Fig. 4.4 indicate the respective "centre of mass"-wavelengths λ_c, as given by

$$\lambda_c = \frac{\sum_i \lambda_i I_i(\lambda)}{\sum_j I_j(\lambda)}, \tag{4.1}$$

where $I(\lambda)$ is the intensity at wavelength λ and the sum is over all measurement points. The centre wavelengths in Fig. 4.4 are 983.4 nm for LD1, 983.3 nm for LD2 and 980.5 nm for LD3.

It can also be seen that each diode oscillates at several modes simultaneously. Due to the irregular shape of the spectrum, it is impractical to use the full width

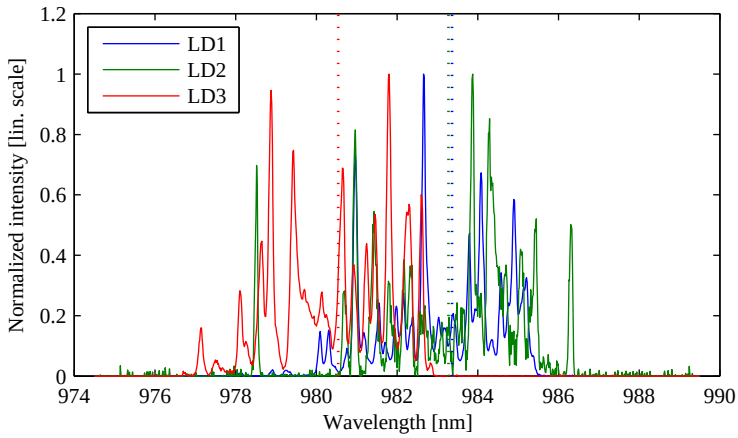

Figure 4.4: Spectra of the pump diodes at 8 A driving current. The dotted vertical lines indicate the centre of mass of the corresponding spectrum (LD1: 983.4 nm, LD2: 983.3 nm, LD3: 980.5 nm).

at half maximum (FWHM) to characterize the output. Therefore, by an analogy with solid mechanics, the spectral width has been defined as the length $\Delta\lambda$ of a thin rod which rotates about the origin, is centred at the centre-of-mass λ_c and has the same moment of inertia as the "mass"-distribution $I(\lambda)$. The mass of the rod and the total mass of the distribution are equal. Hence, the spectral width is given by

$$(\Delta\lambda)^2 = 12\left(\frac{\sum_i I_i\lambda_i^2}{\sum_j I_j} - \lambda_c^2\right), \tag{4.2}$$

where the summation is again done over all sample points. The spectral width at full driving current ranges from approximately 5 nm for LD1 and LD3 to around 6 nm for LD2. At minimum current, the width is reduced by approximately 2.5 nm for all diodes. However, it does not change significantly with the heat sink temperature.

Spectra were recorded for heat sink temperatures from 20 to 30 °C and constant driving current of 8 A. The centre wavelength as function of temperature can be seen in Fig. 4.5. The drift rate is approximately 0.4 nm/°C for all pump diodes. Furthermore, the spectra at constant heat sink temperature of 20 °C were measured for different driving currents. The centre wavelength as function of driving current is shown in Fig. 4.6. The drift rate is approximately 1.6 nm/A for all pump diodes.

Furthermore, Fig. 4.6 shows that the centre wavelength at maximum driving current is approximately 982 nm. To match the centre wavelength of the pumps and the wavelength of maximum absorption in Ytterbium at around 975 nm, the diodes where cooled down to 15 °C, resulting in an emission wavelength of approx-

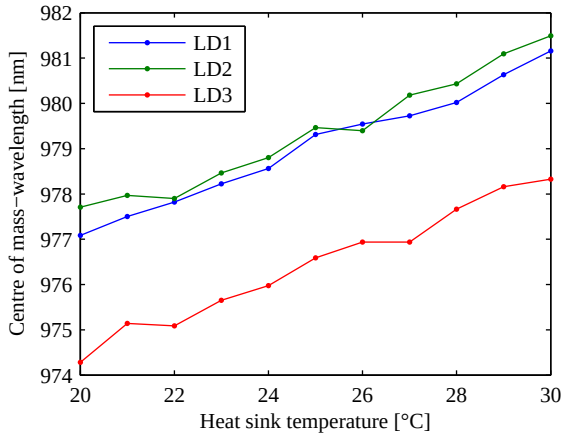

Figure 4.5: Shift of wavelength vs. heat sink temperature. The driving current is 8 A.

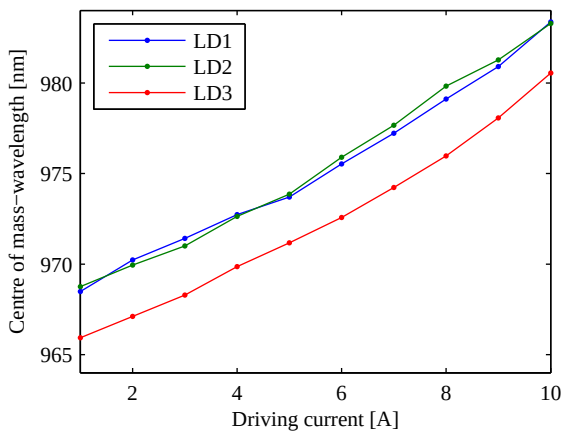

Figure 4.6: Shift of wavelength vs. driving current. The heat sink temperature is 25 °C.

imately 977 nm. It was decided not to cool down further, to avoid extensive water condensation on the heat sink.

Chapter 5

Single Fibre Laser with Broadband Reflector

First, a single fibre laser was built to investigate the performance of the principal setup. Of particular interest was the slope efficiency, the polarization and the quality of the beam. Feedback was provided by a broadband mirror. A schematic drawing of the setup can be seen in Fig. 5.1. The pump light from LD2 was

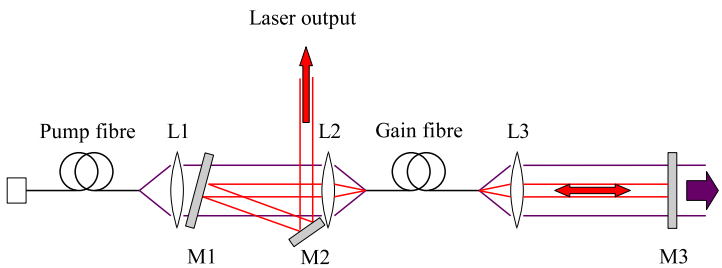

Figure 5.1: Principal setup of the single fibre laser with broadband mirror. The pump light is collimated with lens L1 and focused into the gain fibre with lens L2. High reflection is provided from broadband mirror M3 after the light has been collimated with lens L3. The two mirrors M1 and M2 are used to deflect the laser output and separate the laser from the pump light.

collimated with an aspheric lens of focal length 26.5 mm and then focused into the gain fibre with an identical lens. The gain fibre was ytterbium-doped with a pump absorption of 6.9 dB/m at 980 nm and had a diameter of core and cladding of 10 and 125 µm, respectively (LIEKKI, Yb1200-10/125). Three fibre lengths were investigated, namely 1, 1.5 and 3 m. The fibre was cladding-pumped ($NA_{clad}^{gain} = 0.46$) by a pump diode which was coupled to a delivery fibre with a numerical aperture of $NA_{core}^{pump} = 0.22$. The lenses were arranged such that a 1:1 image of

the pump output is formed on the end of the gain fibre. Both end faces of the active fibre were cleaved perpendicular to the fibre axis. Opposite to the pump end, the fibre output is collimated with another 26.5 mm lens and back reflected with a dielectric dichroic broadband mirror. The mirror has characteristics such that it transmits the pump and reflects the laser light. This side constitutes the highly reflective end of the laser cavity. The cleaved fibre end-face towards the pump is the output coupler. Fresnel-reflections at the glass-air interface give rise to approximately 4 % reflectivity. The emitted light is collimated by the closest lens of the pump arrangement and deflected with another tilted dichroic mirror and one broadband mirror. It was measured that in order to maintain the high transmission for the pump light, the tilt angle of the dichroic mirrors had to be below 3°. The tilt angle which was used in the setup was approximately 2.5°.

The pump diodes were operated at 15 °C heat sink temperature. At this temperature and at maximum driving current, there was a good overlap of the emission spectrum of the pump diodes with the absorption cross section of the gain fibres. Further cooling increased the laser output power even further, however, it was decided to operate at 15 °C to avoid extensive water condensation on the heat sink. All following experiments were performed at this temperature.

Laser Performance

The performance of the fibre laser was assessed by three means. Power measurements were performed to investigate the efficiency of the setup. The spectrum at the laser output was measured with an optical spectrum analyser and the temporal behaviour was recorded with a photo diode and a digital storage oscilloscope.

5.1 Power Performance

One major goal of this thesis is to achieve power scaling by stacking individual fibre lasers. The better the individual laser units are, the more efficient will be the power scaling. Measurements were therefore conducted to investigate the individual laser units in terms of efficiency and optical output power.

The power in the system was measured at three different points in the setup as a function of driving current. The laser output power was measured after deflection from the two outcoupling mirrors. Lossless deflection was assumed. The incident pump power was measured between the pump lenses where the pump beam was collimated. The power of the remaining pump light was measured after the dichroic cavity end-mirror.

Since the coupling into the gain fibre is very sensitive to misalignment, a coupling experiment into an undoped 105/125-fibre was performed to estimate the coupling efficiency. This passive fibre was identical to the pump fibre and it yielded a coupling efficiency of 65 %. The pump beam is assumed to have a Gaussian

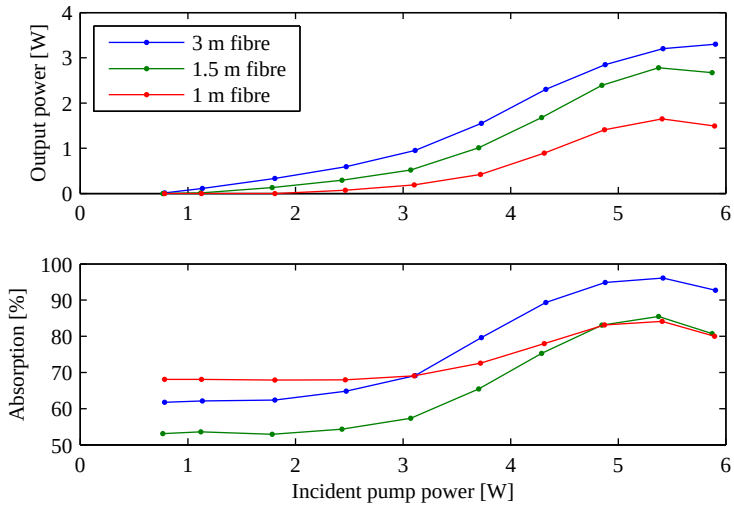

Figure 5.2: Laser performance of different gain fibre lengths with dielectric mirror.

intensity distribution. With

$$\eta_{\text{coupl}} = 1 - e^{-\frac{2a^2}{w^2}} \tag{5.1}$$

one can estimate the coupling efficiency η_{coupl} into a circular aperture, where a is the fibre core radius, w is the beam radius on the fibre end face and reflection losses are neglected [20]. Using Eq. 5.1, the $1/e^2$-spot size diameter of the pump source on the passive fibre was determined to be 145 µm. This is larger higher than the mode field in the pump fibre and was believed to be due to aberrations in the pump optics. Once the pump spot size is known, one can estimate the coupling efficiency into the gain fibre with 125 µm cladding diameter. This yields a coupling efficiency of approximately 80 %.

Fig. 5.2 shows the laser power performance for different fibre lengths with a dielectric mirror for feedback. The maximum output power for the 3 m gain fibre was 3.3 W and was obtained at full incident pump power of 5.9 W. For both the 1.5 m and the 1 m fibre, the output power reaches a maximum at around 5.4 W of incident pump power and then drops again if the pump power was increased further. The drop was due to the shift in pump wavelength which, at full driving current, is beyond the point of maximum absorption of the Yb-fibres. The maximum output powers where 2.8 W and 1.7 W for the 1.5 m and 1 m long fibre, respectively.

The maximum optical-to-optical efficiencies η_{oo} as given by

$$\eta_{\text{oo}} = \frac{P_{\text{l,out}}}{P_{\text{p,in}}}, \tag{5.2}$$

were $P_{\mathrm{l,out}}$ is the laser output power and $P_{\mathrm{p,in}}$ is the incident pump power, were approximately 60 %, 50 % and 30 % for the 3 m, 1.5 m and 1 m long fibres, respectively. It was obtained at the point of highest absorption which was at around 5.5 W incident input power for all fibre lengths. At higher driving currents, due to the shift in pump wavelength, the efficiency decreased accordingly.

The plot of the absorption showed an uncommon behaviour as the absorption for the 1 m long fibre was unexpectedly high at low pump powers (up to ~3 W). To a first approximation, the absorption increases with the fibre length since it is proportional to $e^{-\alpha l}$, where α is the absorption coefficient[1] and l is the length of the fibre. However, repeated measurements showed that the absorption for the 1 m fibre was highest for incident pump powers below 3 W. This was believed to be due to inhomogeneities in the doping concentration along the fibre. This was supported by following experiments were fluorescence of different intensities was observed for two fibres of same length and at an identical pump level.

The laser threshold increases with decreasing fibre length. The measured values for the 3 m, 1.5 m and 1 m long fibres are 1 W, 1.6 W and 2 W of incident pump power, respectively.

The power characteristics of the different fibre lengths are summarized in Fig. 5.3.

5.2 Spectrum

Depending on the application, the requirements for the output spectrum of the laser can be very demanding. If the beam has to be frequency-converted, the laser needs to have a very narrow linewidth, while a broad spectrum might be sufficient in an application that requires only high output power. The spectrum was therefore measured with an optical spectrum analyzer (OSA).

The lasers were not frequency-locked, therefore, they operated on the spectral gain peak. It can be seen in Fig. 5.4 that the spectrum shifts towards shorter wavelengths as the fibre length is decreased. This is a consequence of the quasi-3-level nature of Yb, in which the spectral absorption and emission cross sections overlap. The gain $g(\lambda)$ of a laser system with population concentrations of the upper and lower laser level N_{u} and N_{l} and emission and absorption cross-sections $\sigma_{\mathrm{em}}(\lambda)$ and $\sigma_{\mathrm{abs}}(\lambda)$ is given by:

$$g(\lambda) = N_{\mathrm{u}}\sigma_{\mathrm{em}}(\lambda) - N_{\mathrm{l}}\sigma_{\mathrm{abs}}(\lambda) \tag{5.3}$$

Hence, with different inversion $(N_{\mathrm{u}} - N_{\mathrm{l}})$ the gain spectral peak shifts, meaning that changing the fibre length can lead to significant shifts in the output spectrum as can be seen in Fig. 5.4.

[1] The absorption coefficient is determined by the absorption cross-section of the dopant and the population inversion, which decreases as the fibre gets longer. However, for sufficiently high pump powers, the change in inversion is not very high and hence, the overall absorption decreases for shorter fibre lengths.

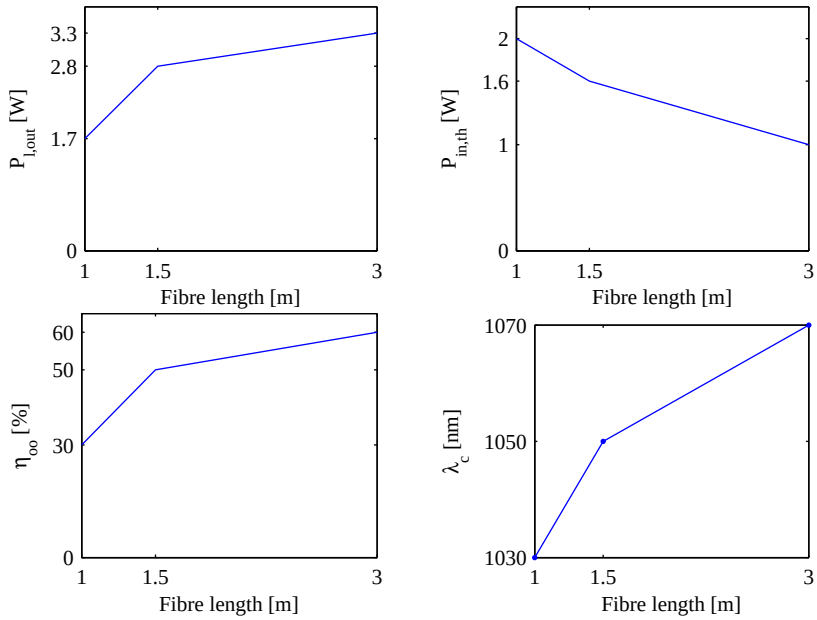

Figure 5.3: Laser output power $P_{\mathrm{l,out}}$, incident pump power threshold $P_{\mathrm{abs,th}}$, optical-to-optical efficiency η_{oo} and centre frequency λ_c vs. fibre length.

The centre wavelength as calculated with Eg. 4.1 shifts from 1070 nm for the 3 m fibre, over 1050 nm for the 1.5 m fibre to 1030 nm for the 1 m fibre. The output spectra were generally unstable and small side peaks appeared and vanished irregularly between consecutive measurements. The spectral widths in Fig. 5.4 were 4 nm, 30 nm and 10 nm for the 3 m, 1.5 m and the 1 m long fibre, respectively.

5.3 Self-Pulsing

A common phenomenon for Yb-doped fibre lasers is that they can exhibit strong self-pulsing. This effect is mostly undesired since the peak powers during such a pulse can reach intensities which might damage components inside the laser cavity or even the gain fibre itself. The origin of self-pulsing is not yet fully understood, however, the two existing pulsing phenomena, pulses which are either produced at the frequency of the relaxation oscillations or at the inverse of the cavity round trip time, can both be described as interactions of the laser signal with the population inversion [21, 22].

To investigate the temporal behaviour of the laser output, the laser beam was

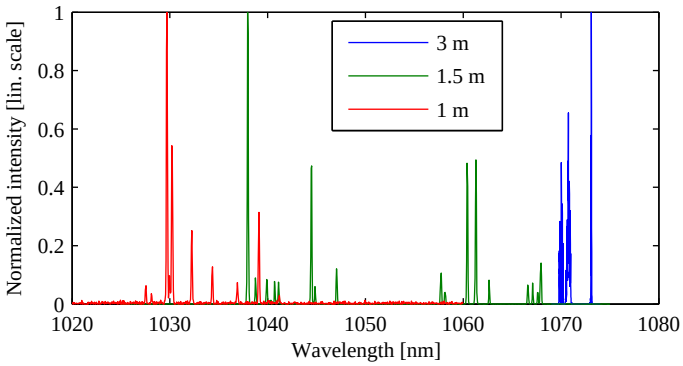

Figure 5.4: Spectra for three different fibre lengths with dielectric cavity mirror. The spectra shift towards shorter wavelengths as the fibre length decreases, since the gain peak of the laser changes with inversion.

aimed at a fast photo diode (Hamamatsu, InGaAs PIN photo diode with 3 GHz cut-off frequency) and the diode signal was measured with a digital storage oscilloscope (Tektronik TDS 5104). The output was measured at laser threshold, at maximum pump power and at an intermediate pump level. Three waveforms were recorded at each pump power to show different features of the laser output. The waveforms for the 3 m long gain fibre at 3.5 W absorbed pump power are shown in Fig. 5.5 and characteristic times for the pulse separation (τ_1), the pulse width (τ_2) and self mode-locking (τ_3) are indicated.

Self-pulsing starts already at laser threshold. There is no cw-contribution to the laser output and all the energy is contained in the pulses. The pulse repetition rate is 20 kHz at threshold (0.4 W) with a pulse width of approximately 3 µs. The pulses are modulated by even smaller pulses which are separated by around 30 ns. For a 3 m long fibre, this corresponds to the cavity round trip time, hence this fibre laser also exhibits self mode-locking.

At higher absorbed pump powers the separation of the main pulses becomes smaller. The repetition rate at 2.2 W is approximately 220 kHz, whereas it is around 290 kHz at maximum absorbed power of 4.1 W. The pulse width decreases from 0.8 µs at 0.4 W to around 0.3 µs at full pump power.

A comparison between the three different fibre lengths is shown in Fig. 5.6. It can be seen that the pulse frequency increases with decreasing fibre length. Both shorter fibres have a pulse repetition rate of approximately 500 kHz at full pump power. The pulse width, however, decreases similarly for all three fibres from around 3 µs at threshold to approximately 0.5 µs at full pump power. From the recorded waveforms, one can also determine the modulation M of the laser output. As shown in Fig. 5.7, it is defined as the amplitude $\hat{I}$ of the modulation divided by the mean

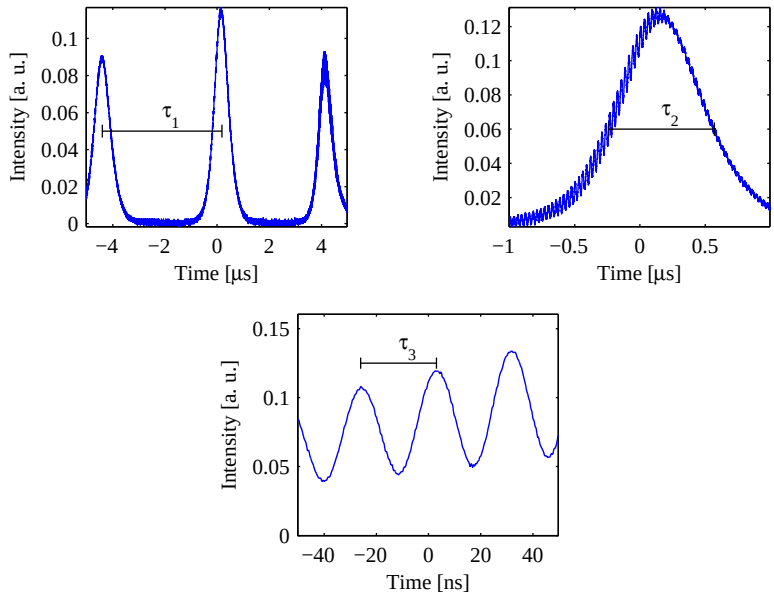

Figure 5.5: Temporal behaviour of the laser output with 3 m gain fibre at 2.2 W absorbed pump power. Characteristic times for the pulse repetition rate ($1/\tau_1$), pulse width (τ_2) and self mode-locking (τ_3) are indicated.

of the signal $\bar{I}$. Hence, the modulation is given by

$$M = \frac{I_{\max} - I_{\min}}{I_{\max} + I_{\min}}, \tag{5.4}$$

where $I_{\max}$ and $I_{\min}$ are the maximum and minimum intensity of the modulated signal, respectively.

The modulation for the 3 m fibre is constantly 1. This means that there is no cw-contribution in the signal and the output is purely pulsed. The behaviour improves as the fibre length decreases. The 1 m fibre has a modulation of approximately 20 % if it is operated at maximum pump power, approximately 3 times above threshold. However, one should note that the output was unstable and the values were varying throughout the measurement. E. g. for the 1.5 m fibre, the output switched from regimes with purely pulsed output to less modulated behaviour in intervals of up to 5-10 s. Therefore, the values for the modulation (Fig. 5.6) are only approximate numbers. However, at low pump powers where the gain is not depleted, strong pulsing will occur independent of the fibre length.

The spectral, temporal and power characteristics of the different fibre lengths are summarized in Tab. 5.1.

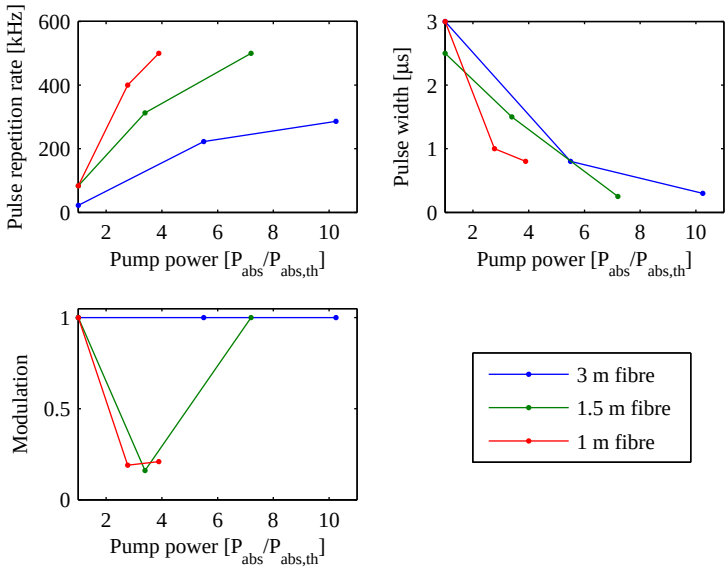

Figure 5.6: Temporal behaviour of the laser output vs. normalized absorbed pump power for three different gain fibre lengths.

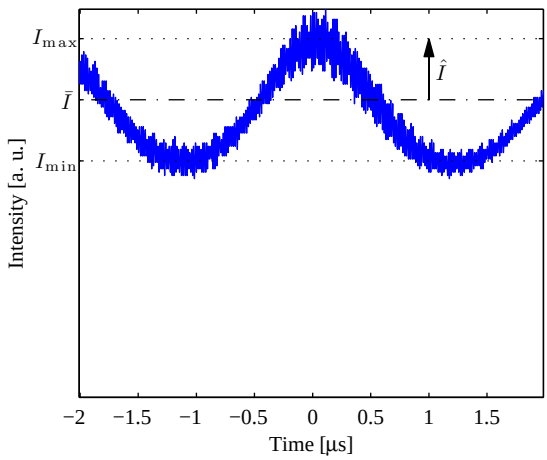

Figure 5.7: The modulation is defined as the modulation amplitude $\hat{I}$ divided by the mean of the signal $\bar{I}$. The figure shows the signal of the 1 m gain fibre two times above threshold.

Table 5.1: Summary of laser characteristics for different fibre lengths.

Fibre length [m]	$P_{\mathrm{in,th}}$ [W]	P_{max} [W]	η_{oo}	λ_{c} [nm]	M at P_{max}
3	1.0	3.3	0.6	1070	1.0
1.5	1.6	2.8	0.5	1050	1.0
1	2.0	1.7	0.3	1030	0.2

5.4 Beam Quality

One possible application of the laser array is in laser writing. Hence, the beam quality of the single laser is of high importance. This was assessed by means of the beam's M^2 factor. For this measurement, a razor blade was moved through the beam after a focussing with a lens and the positions of the blade were measured when it removed 16 % and 84 % of the total beam power. These positions of the blade correspond to distances of $\pm\frac{1}{2}w$ from the beam's main propagation axis. The points were fitted to Eq. 2.14 and the corresponding M^2 value was obtained.

Since the M^2 value was expected to depend only on the transverse dimensions of the fibre and the output coupling, the measurement was conducted only on the 3 m long fibre. The results can be seen in figure 5.8. The M^2 factor was approximately 5. This is a large value since usually, fibre lasers approach $M^2 \approx 1$ rather easily.

The high value was primarily due to higher order modes in the fibre which give rise to a larger divergence angle of the beam. This was supported by visual inspection of the beam profile where a non-Gaussian shape was sometimes observed. However, the fibre's V-number of 2.44 is very close to the single mode condition $V \leq 2.405$, hence, a large number of higher order modes should not be supported.

Another possibility for the high M^2 factor is a poorly cleaved fibre end-face. This is supported by later experiments, where different M^2 factors where measured

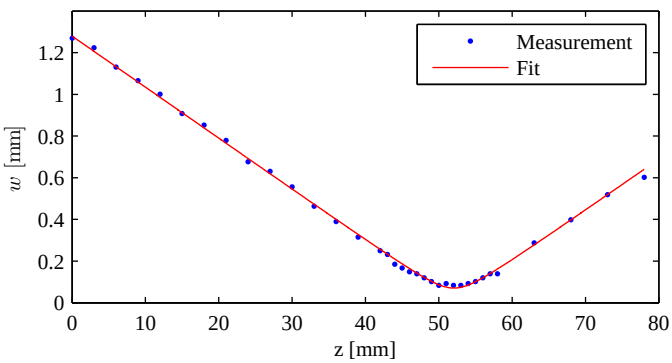

Figure 5.8: Measurement of the beam diameter and fit for the M^2 factor of the 3 m fibre. The measurements yielded a M^2 factor of 5.

for three different fibres. These fibres where all cut from the same reel, which excludes variations in fibre geometry due to the manufacturing process.

The lenses on the output coupling side of the fibre were assumed to introduce no significant aberrations.

Chapter 6

Single Fibre Laser with Polarized Output

For some applications, e. g. lithography, it is required to convert the laser output to shorter wavelengths. This can only be done efficiently if the beam is linearly polarized. Therefore, the gain fibre was chosen to be polarization maintaining, which, together with a polarization-selective element allows to obtain a linearly polarized laser output. The principal setup that was used can be seen in Fig. 6.1. The polarizer inside the laser cavity (denoted P1 in Fig. 6.1) was of Glan-Taylor

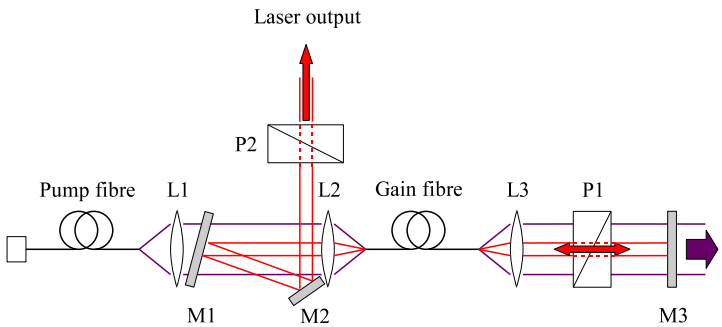

Figure 6.1: Principal setup with polarizer inside the cavity (P1). Polarizer P2 was used to measure the polarization extinction ratio.

type and was used to introduce high loss in one of its polarization directions. P2 was a Glan-Thompson polarizer and was used to measure the polarization extinction ratio of the output beam.

The measurement was performed by stepwise rotating the inner polarizer P1 and for each rotation step, the minimum and maximum output power was determined during one full revolution of the outer polarizer, P2. The polarization extinction ratio (PER) is then defined as ten times the decimal logarithm of the ratio of the

minimum and maximum power, $P_{\min}$ and $P_{\max}$.

$$\mathrm{PER} = -10 \log_{10} \left(\frac{P_{\min}}{P_{\max}} \right) \tag{6.1}$$

The measurement was performed with the 1 m gain fibre using the highly reflective dielectric mirror for feedback. The maximum output power without the external polarizer was around 1.8 W.

The results of the measurement are shown in Fig. 6.2. The graph shows two clear peaks. They occur when the transmission axis of the polarizer and the fast axis of the PM fibre coincide. The best polarization extinction ratio was approximately 12 dB. This corresponds to a ratio $P_{\min}/P_{\max}$ of around 0.06. The most stable output was found at rotation angle 300°. Other orientations resulted in an unstable output were the polarization direction jumped between different states. This made the manual measurement difficult to perform which resulted in large uncertainties for PER values below 5, as indicated by the error-bars in Fig. 6.2.

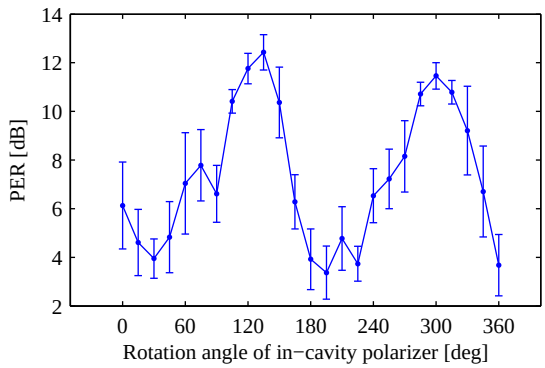

Figure 6.2: Polarization extinction ratio vs. rotation angle of in-cavity polarizer.

If linearly polarized light is launched into a PM fibre, its polarization direction is maintained if the polarization direction is along either one of the birefringent axis of the fibre. Therefore, it was expected that four peaks are visible in Fig. 6.2 which was clearly not the case. This was believed to be because of parasitic lasing on the cleaved end faces of the fibre. Cleaved end faces can create a sub-cavity inside the laser without a polarization selective element. Hence, it will produce unpolarized laser light regardless of the orientation of polarizer P1 and will thus result in a lower PER value.

This hypothesis was supported by later experiments (chapter 8) in which the fibre end faces were angle polished to suppress parasitic lasing. In these experiments, a linearly polarized laser output was obtained even if the light was launched into the fibre with its polarization direction along the slow axis of the fibre.

6.1 Laser Performance

The laser performance was slightly superior to the laser without polarizer, the maximum output power was approximately 1.8 W. This was obtained with the transmission axis of the in-cavity polarizer being along the fast axis of the gain fibre, which corresponds to a rotation angle of 300° in Fig. 6.2. With 40 % maximum optical-to-optical efficiency, it outperformed the unpolarized laser by almost 30 %. This is somewhat unexpected since the polarizer introduces additional losses due to reflections from its calcite surface. The most probable reason for the improved performance is poor alignment in the previous experiment. The results can be seen in Fig. 6.3. For comparison, the power performance for the unpolarized 1 m fibre is added to the figure.

In a Glan-Taylor polarizer, the incident beam is split up in an ordinary and an extraordinary ray. The extraordinary ray is transmitted through the polarizer while the ordinary ray is deflected. For assessing the laser performance, only the laser light which was transmitted through the polarizer was taken into account. The deflected laser light was in the order of 30 mW and was neglected. However, both beams of the pump light were considered for calculating the absorption.

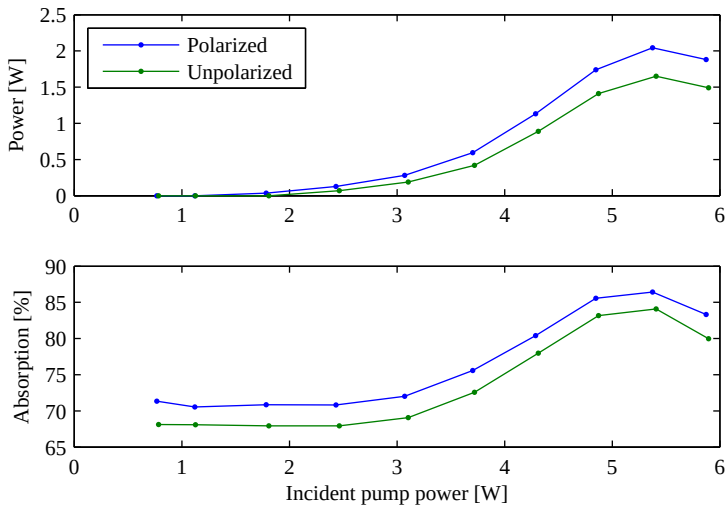

Figure 6.3: Laser performance with 1 m gain fibre and broadband reflector. The linearly polarized laser (blue) yielded higher output power than the same setup without polarizer (green).

The temporal behaviour was similar to the 1 m fibre without polarized output. The output was temporally unstable and regimes of purely pulsed behaviour changed into outputs were a modulation as low as approximately 15 % was mea-

sured. Compared to the unpolarized 1 m fibre, good agreement was observed in terms of pulse width and repetition rate.

Chapter 7

Single Fibre Laser with Volume Bragg Grating and Polarized Output

To obtain efficient frequency conversion with nonlinear crystals such as periodically poled potassium titanyl phosphate (PPKTP), a narrow spectral width of the laser beam is required. Broadband reflectors are not able to provide this. Therefore, the fibre laser was frequency-locked with a volume Bragg grating (VBG). The principal setup was identical to that of the polarized laser in Fig. 6.1, except that the broadband mirror M3 was replaced by a VBG with a reflection bandwidth of 0.5 nm (FWHM). The output from the fibre was collimated with a lens of 26.5 mm focal length, which gives a $1/e^2$-spot diameter on the grating of approximately 4 mm.

The operating conditions were the same as for the previous lasers, i. e. the pump diode temperature was 15 °C, the end faces of the gain fibre were cleaved and the transmission axis of the in-cavity polarizer was aligned such that the polarization direction of the transmitted light coincided with the fast axis of the PM fibre.

7.1 Laser Performance

The power performance of the 1 m gain fibre with VBG and linearly polarized output can be seen in Fig. 7.1. It was assumed that the same amount of pump light was deflected in the polarizer as for the laser with dielectric mirror (see chapter 6). The maximum laser output power was approximately 1.5 W. This was around 20 % less than the output from the equivalent laser with the dielectric reflector. The maximum optical-to-optical efficiency was around 25 %.

The laser wavelength was locked at 1029 nm and had a spectral width (FWHM) of approximately 0.1 nm. Small side peaks, probably due to parasitic lasing on the cleaved intra-cavity fibre end-faces, appeared irregularly at longer wavelengths but could be suppressed effectively by bending the fibre around a post with 50 mm

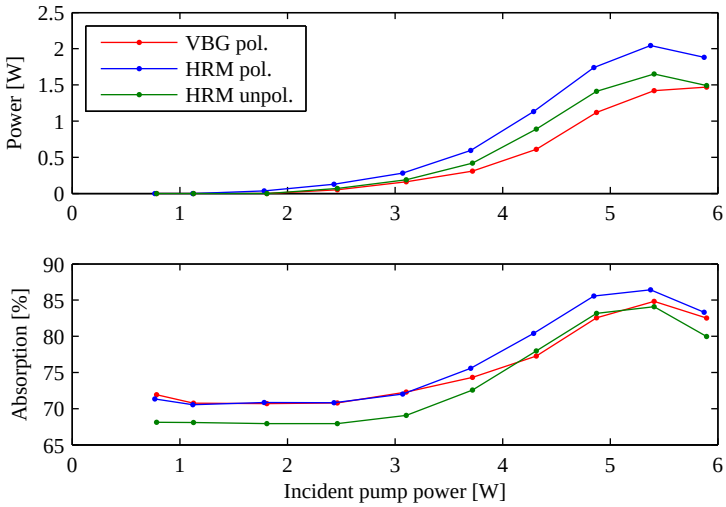

Figure 7.1: Performance of different lasers with 1 m gain fibre length.

diameter. The spectrum is shown in Fig. 7.2, together with the spectrum of the laser with the dielectric mirror for feedback.

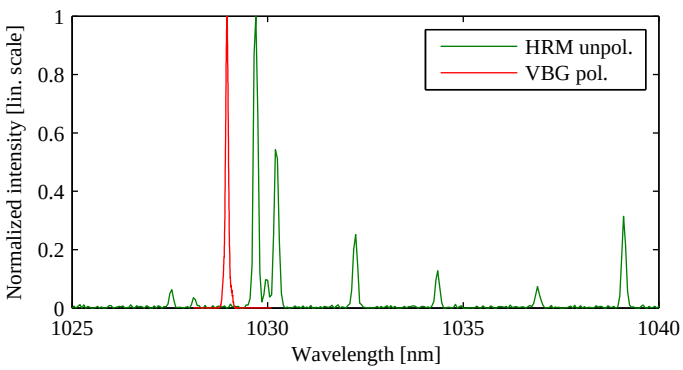

Figure 7.2: Spectrum of 1 m gain fibre with VBG and dielectric mirror (HRM) for feedback. The FWHM of the VBG-locked spectrum is 0.1 nm and was centered around 1029 nm.

The performance in terms of linear polarization was worse than the comparable laser with dielectric reflector. The polarization extinction ratio was only around 10 dB and the output was more unstable and the state of polarization was changing faster and stronger. Similarly to chapter 6, this can be attributed to parasitic lasing

on the cleaved fibre end-faces in the intra-cavity.

7.2 Self-Pulsing

Measurements were also performed to investigate self-pulsing. The laser showed strong self-pulsing with 100 % modulation at all pump levels. This deviated from the behaviour of the lasers with broadband mirror were a modulation of around 20 % was measured.

This was believed to be because of stimulated Brillouin scattering which acted as the seed for the onset of self-pulsing [21, 23]. Brillouin scattering is an interaction of the optical field with acoustic phonons via electrostriction [16]. During this process, a periodic modulation of the refractive index is created along the waveguide, from which the incident beam is back reflected. Thus it was expected that a spectrally well-defined incident beam, which was locked with a VBG, would create a index variation with high reflectivity and hence, Brillouin scattering would be increased [24].

This was supported by following experiments with a 2 m long fibre, where a temporally stable, purely pulsed output was observed.

Chapter 8

Fibre Laser Array

In the preceding chapters, lasers with a single gain fibre were built and their outputs were analysed. Their behaviour is now well-known so that from here on, focus will be put on the fibre laser array. First, several changes to the setup will be introduced, then the performance of the system with three parallel fibre lasers will be investigated.

As shown before, self-pulsing was observed for all fibre lengths independent of the cavity mirror. Since it will depend on the application whether or not self-pulsing can be tolerated, it was decided to build the array such that the power output was maximized.

Previous measurements showed an increase in output power as the gain fibre length was extended. The fibre laser array was therefore built with the longest fibres available, namely three pieces, each with a length of 2 m. The principal setup is shown in Fig. 8.1, but for clarity only with one gain fibre.

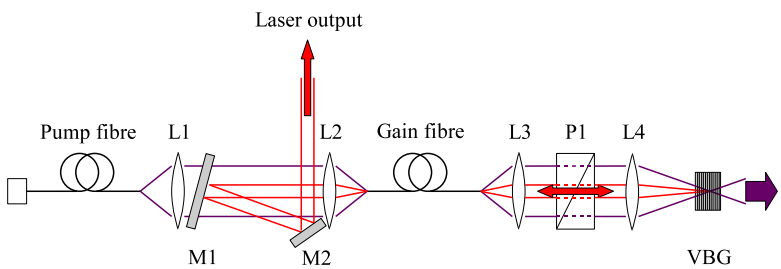

Figure 8.1: Setup of the fibre lasers as used in the array setup. The configuration of the lenses L3 and L4 allows feedback from the VBG also for the off-axis fibres.

The laser setup in the previous chapters was built such that the symmetry

axis of the fibre and the optical axis of the collimating lens coincided. In such an arrangement, the collimated laser beam will impinge on the cavity mirror at normal incidence and is therefore back reflected into the core of the gain fibre.

However, this works only if the fibre axis is along the optical axis of the lens. A lateral offset of the fibre will still give a collimated output, but the beam will no longer propagate along the optical axis of the system. The laser beam will impinge on the VBG at oblique incidence and the back reflected beam will not be coupled back into the fibre core. Moreover, VBGs are sensitive to the angle of incidence, the reflection properties will change accordingly.

The lens arrangement was therefore changed into an afocal system, where the lenses were separated by the sum of their focal lengths. The lenses were placed such that the front focal plane of the first lens was on the fibre end face. The image was then formed in the back focal plane of the second lens, which is where the VBG was placed. Such a system gives back reflection independent of the fibre offset from the optical axis. The path of rays is illustrated in Fig. 8.2.

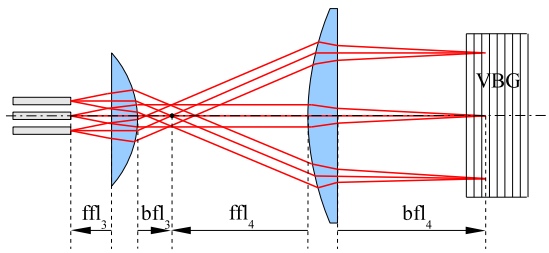

Figure 8.2: In this optical system, the back focal plane of the first lens and the front focal plane of the second lens coincide. Such an arrangement has infinite effective focal length, hence, it is afocal. It allows for collinear propagation of the fibre output after imaging through the system.

If the incident light on a VBG is a plane wave, then the reflection is basically limited by the properties of the grating, e. g. the strength of the index modulation or the length of the grating. However, the reflection will decrease if the beam is focussed into the VBG and the angular spread of the beam is larger than the acceptance angle of the grating. It was shown in [25] that reasonable reflection can still be obtained if the following condition (for normal incidence) is fulfilled:

$$A = \frac{\pi^2}{4} n_0^2 \frac{w_0^2}{\lambda_B^2} \frac{\Delta\lambda}{\lambda_B} > 1 \tag{8.1}$$

The quantities λ_B and $\Delta\lambda$ denote the Bragg wavelength and the reflectivity bandwidth of the grating, w_0 is the beam waist and the glass has refractive index n_0. Therefore, the lenses were chosen such that a beam waist of approximately 24 µm

was formed inside the grating. The lenses had focal lengths of $f_3 = 8$ mm and $f_4 = 38.5$ mm, respectively, yielding an A-parameter of 1.4.

The first lasers often showed parasitic lasing on the end faces of the gain fibres. This was suppressed by angle polishing the fibre ends at the side where the VBG was placed to 7°. The light which is guided in the core is then back reflected from the inclined surface at an angle which is larger than the acceptance angle of the fibre core. It is therefore coupled out into the cladding and hence, parasitic lasing is reduced.

Fibre Alignment

Once the fibres are aligned on the setup, there is no possibility to adjust the components for the individual lasers. Hence, alignment of the individual fibres is crucial. A holder was therefore built, where the fibres could be positioned accurately. As shown in Fig. 8.3, it consisted of an aluminium block onto which three V-grooves were milled in which the fibres were placed. The separation and depth of the grooves was specified to be 300 µm and 50 µm, respectively. Two holders where used to position the gain fibres, one at the highly reflective cavity-end (for convenience referred to as the VBG-side of the fibres, right column in Fig. 8.4) and another one at the out-coupling end (left column in Fig. 8.4). Another identical holder was used to position the three pump fibres. Each one was used to pump one individual gain fibre through simultaneous 1:1 imaging of their fibre end-faces onto the gain fibres. The holders were cleaned with acetone in an ultrasonic bath, to avoid particles in the V-grooves which would result in poor alignment and to remove fat and other liquids through which light could be coupled out from the uncoated cladding.

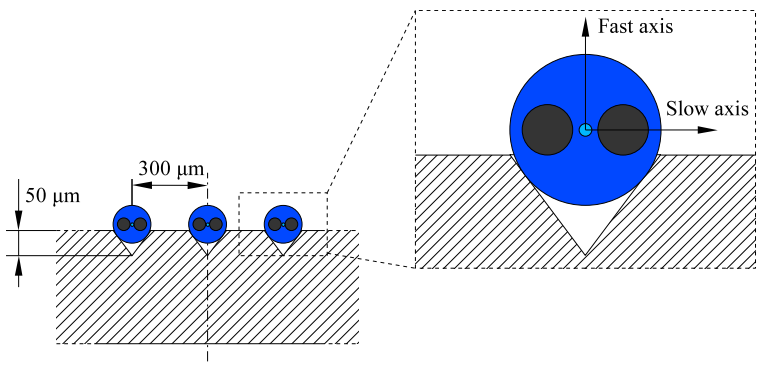

Figure 8.3: Positioning of the fibres on the holder. The stress elements were aligned in the plane of the table.

The front face of the fibres after alignment is shown in Fig. 8.4. It can be seen that the cleaving was not perfect, some points of rupture are visible around the edge

of the fibre. However, the area in the vicinity of the core showed no degradation. Blue light was coupled in from the back end of the fibre with a LED for better visualization of the stress elements.

Lateral positioning could be achieved with fairly good accuracy, all fibres where spaced by 310 µm, except for fibres 3 and 2 on the out-coupling side, where the spacing was only 290 µm, as shown in Fig. 8.4. The depth of the V-grooves was the same for all fibres and no significant deviation could be measured.

The axial placing was done by moving the fibres with a translation stage while visually inspecting their position with a microscope. As shown in Fig. 8.4, there is a displacement between fibres 1 and 3 on the out-coupling side, with an offset of approximately 30 µm. However, the axial displacement is not expected to cause a large drop in performance. This is because due to the numerical aperture of the delivery fibre ($NA_{core}^{pump} = 0.22$) and 1:1-imaging from the coupling optics, the focussing angle of the pump beam is fairly small (NA= 0.22). Therefore, the distance from the focus after which the pump spot diameter has significantly increased, e. g. by factor $\sqrt{2}$, is more than 130 µm. Hence, no significant coupling losses are expected, if the misalignment is well below this distance. There is no axial displacement on the VBG-side of the array, since all fibre ends where polished to the exact same length simultaneously.

A device was built for adjusting the rotation angle of the fibres. The rotation angle was monitored by coupling light from a He-Ne laser into the opposite end of the fibre end under inspection. The illuminated front face was then imaged with a lens of focal length 10 mm onto a wall, approximately 3 m away. This gave rise to an image diameter of around 40 mm, which was in turn used to rotate the fibre to the desired position. The alignment could be done with an accuracy of around $\pm 10°$. The fibres were aligned such that the stress elements, and hence, the slow axis of the birefringent fibre, were in the plane of the table.

It should also be noted that the method which was used cannot allow for perfect alignment. This is because due to intrinsic stress in the fibres, one of the axes of birefringence does not necessarily coincide with the axis through the geometric centres of the stress elements.

After moving and rotating the fibres into position, they were fixed in the grooves with a small drop of varnish. The varnish must only be in contact with the fibre coating since otherwise, if the the glue has a sufficiently high refractive index, light will leak out of the fibre at the glass-varnish interface. A varnish was preferred instead of epoxy resin, because even though it is less durable, cleaning the grooves for realignment was easier. The outer fibres were positioned first, in order to avoid remnants of the varnish to flow over and contaminate the neighbouring grooves. The alignment was monitored during hardening, because the varnish contracted as its solvent evaporated. After the varnish had dried, the fibres were clamped into the grooves from above with a metal plate.

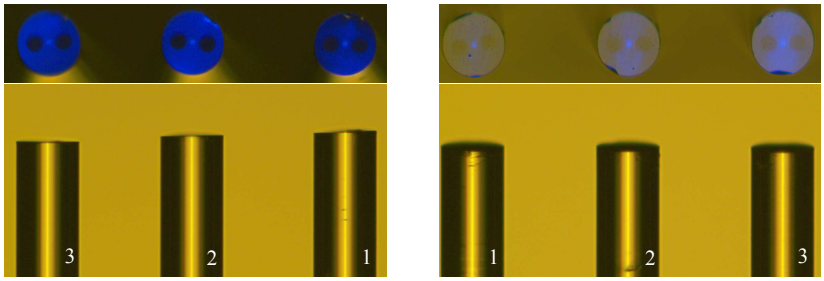

Figure 8.4: Fibre ends after alignment. The images to the left show the cleaved fibre ends, the right side shows the fibre ends which were angle polished to 7°. The end faces were not perfectly cleaved, however, the area around the fibre core showed no degradation.

8.1 Individual Laser Performance

The lasers have different fibre lengths compared to the previous experiments, therefore, the individual lasers were investigated at first. As shown in Fig. 8.5, the maximum output powers were 2.5 W, 3.3 W and 3.1 W for fibres 1, 2 and 3, respectively (nomenclature according to Fig. 8.4). This is in between the performance of the 3 m and 1.5 m long gain fibres, as expected. The measurement was performed without readjusting and maximizing the individual laser outputs, hence, the power of the array scaled linearly with the number of individual lasers in the setup. All lasers showed self-pulsing at all pump levels.

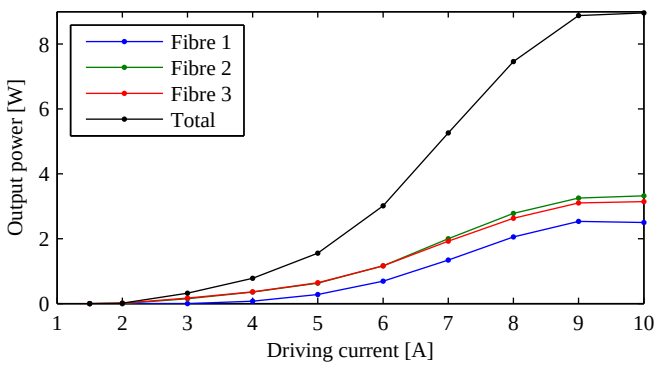

Figure 8.5: Power output of the individual lasers in the array setup. The lasers were operated in parallel without individual readjustment, hence, the power of the array scaled linearly with the number of individual lasers.

As shown in Fig. 8.6, the wavelength of the central fibre was locked at 1029.1 nm and the off-axis fibres were differing by not more than 0.1 nm. The spectral full widths at half maximum were approximately 0.08 nm. This indicates that the

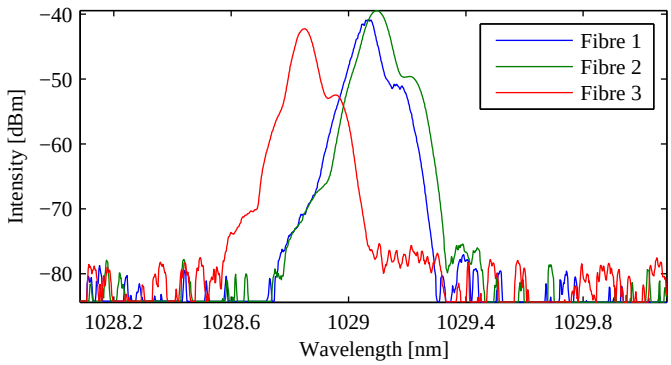

Figure 8.6: Spectrum for all fibres on the array setup without individual readjustments. The slight wavelength-shifts are believed to be mostly due to inhomogeneities in the grating period.

grating has an inhomogeneous grating pitch over its aperture. To some smaller extend, the temperature distribution through the grating and an oblique angle of incidence of the beams from the outer fibres can lead to a further shift in wavelength.

The polarization extinction ratios were 23 dB, 13 dB and 15 dB for fibres 1, 2 and 3, respectively. The deviation from one fibre to the other is because all lasers use the same polarizer as their polarization selective element. Therefore, if the fast and slow axis of the fibres are not parallel, poor alignment will immediately result in a lower PER for some fibres. Since parasitic lasing was reduced by angle polishing of the end faces, good PER-values could be obtained even though the transmission axis of the polarizer in this setup was aligned with the slow axis of the PM fibre (compare to the measurement in chapter 6).

The M^2 factor of the fibres were 1.2, 2.2 and 5.2 for fibres 1, 2 and 3, respectively. This variation is quite large and no satisfying explanation for the poor performance of fibres 2 and 3 was found. The measurement on fibre 3 was repeated due to the large fluctuations in output power, however, similar results were obtained.

As stated in chapter 5, the poor beam quality was believed to be due to higher transverse modes in the fibres as indicated by visual inspection of the laser spot. Furthermore, a poor output coupler could also degrade the beam quality, e. g. if debris settled on the fibre end faces or if microscopic cracks were created when the fibres were cleaved. A poor output coupler would also provide an explanation for the breaking of two fibres at a later point, as dirt on the end face can create a hot-spot which introduces high stress in the silica glass.

8.2 Array Performance

To compare the performance of the array in terms of beam profile with the simulation from chapter 3, the intensity distribution of the output was measured with a scanning-slit beam profiler (DataRay Inc., BeamScope-P5).

The total power impinging on the profiler had to be lowered, therefore, the measurement was conducted on the reflection of the beam from a glass plate as shown in Fig. 8.7. In order for the beams to propagate collinearly, two afocal lens arrangements had to be used, one before (lenses L2 and L5) and one after the reflection (lenses L6 and L7). The lenses where chosen, such that the total magnification of the imaging system was approximately 2, namely $f_2 = 26.5$ mm, $f_5 = 75$ mm, $f_6 = 75$ mm and $f_7 = 50$ mm. Distances in the image plane are therefore twice as large as in the object plane, angles, on the other hand are half the size. Hence, the plane of interest is four times the distance from the image plane compared to the simulation from chapter 3. If necessary, an aperture was placed in the intermediate image plane to block one of the beams.

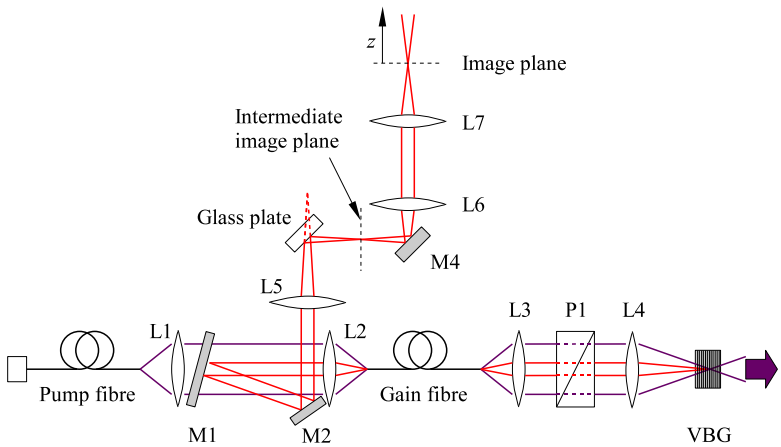

Figure 8.7: The measurement of the beam profile was conducted on the reflection of the beam. The fibre ends were imaged with two afocal lens arrangements (L2+L5 and L6+L7) to yield a total magnification of 2.

The lasers were pumped with around 6 W, since at this power the peak intensity of all lasers was approximately the same. At full pump power, the laser output powers were different from fibre to fibre, due to the different spectra of the pump lasers and hence, different pump efficiencies.

Because of a broken pump diode, not all lasers could be operated at the same time. Therefore, the outer two beams were scanned at first, and the central profile was measured separately and added afterwards. One single scan with the beam

profiler recorded the intensity distribution along the $x-$ and $y-$direction. For each beam, several scans were performed at different positions along z. They were recorded over the region of z where, according to Fig. 3.1, the desired modulation of the beam profile was expected.

Figs. 8.8(a) and 8.8(b) show the profiles of only the central beam at $z = 4$ mm. Fig. 8.8(a) shows the cross-section of the profile in x-direction, whereas Fig. 8.8(b)

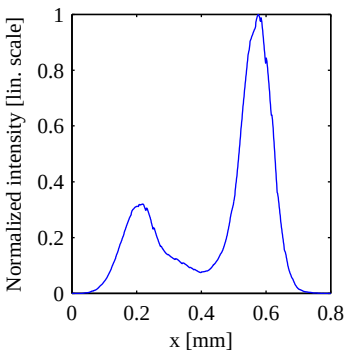

(a) Measured intensity profile in x-direction.

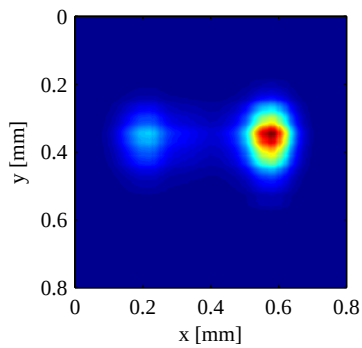

(b) Reconstructed 2D-intensity profile from x- and y-scans.

Figure 8.8: Beam profile from the central fibre at $z = 4$ mm. The small side-peak on the left in both images is an artefact from the measurement. In this example, the peak intensity of the artefact is 30 % of the overall maximum value.

shows a 2D profile of the same beam, which was reconstructed from the profiles in both, $x-$ and $y-$direction.

Both images show a small side peak to the left of the main peak, which was not observed in the real laser beam. It was an artefact from the measurement with the beam profiler. Even though the side peak amplitude was low, it did contribute to the amplitude of the neighbouring main peak as can be seen in Fig. 8.9, e. g. at $z = 8$ mm.

Fig. 8.9 shows the measured total intensity distributions for different positions along the propagation direction (blue line). The individual beams are indicated by the red lines. It can be seen that only the beams from fibres 1 and 2 propagated collinearly. The third beam diverged at an angle of approximately 0.5°. Hence, the separation of the outer peaks changed from approximately 0.55 mm close to the image plane, to around 0.7 mm after 20 mm of propagation. This can firstly be attributed to poor cleaving of the fibre end faces and furthermore be a result of non-parallel V-grooves on the fibre holder. The error-contribution from the lateral misalignment of the fibres (alignment error of approx. 7 %, see Fig. 8.4) is negegible.

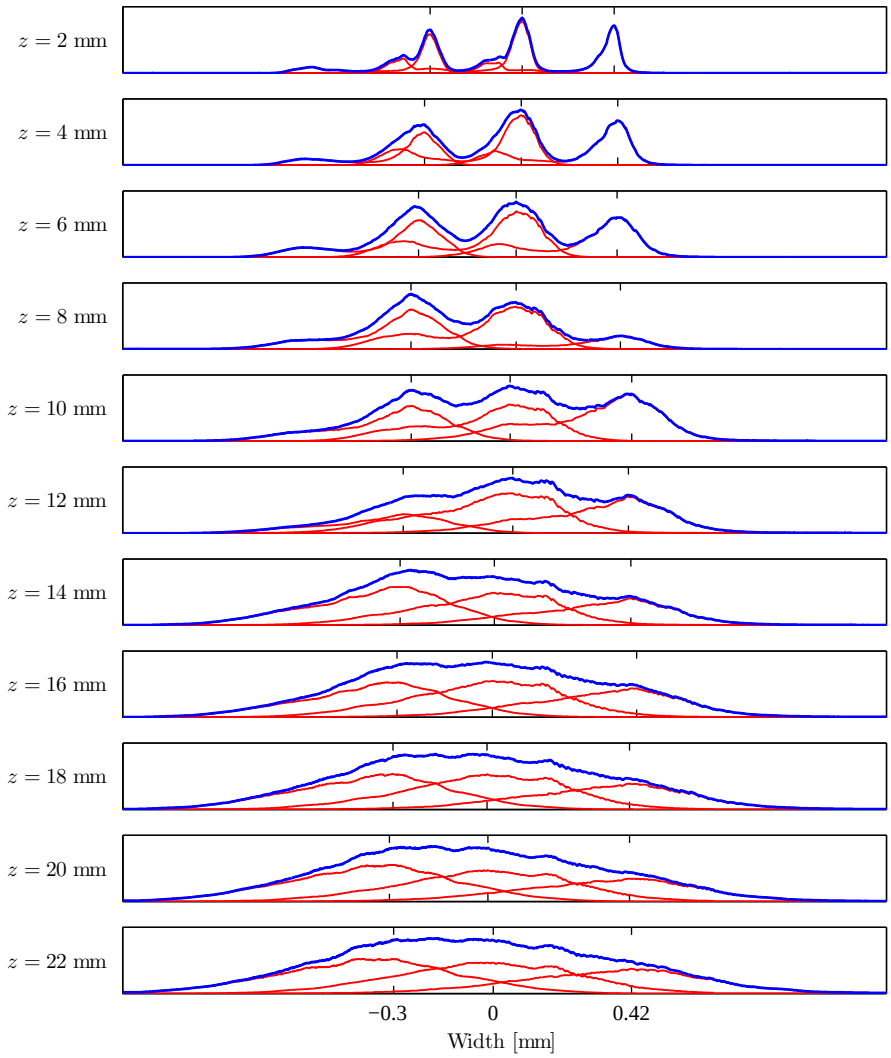

Figure 8.9: Measured total intensity distributions for different positions along the propagation axis (blue). The axis ticks indicate the peak intensities of the single beams (red) as recorded from the individual beam scans.

Furthermore, the output power of the lasers, in particular, the laser to the right in Fig. 8.9, changed during the measurements. The maximum intensity of the beams was therefore not equal for all z-positions and hence, the overall beam profile deviates from the simulation more or less pronounced as the beam propagates along z. An example for a good profile in Fig. 8.9 is e. g. given at $z = 10$ mm, whereas a poor beam can be seen at $z = 8$ mm.

Considering the uneven outputs and focussing more on the left half of the profiles, a beam with the desired line-like profile is given between approximately $z = 16$ mm and $z = 18$ mm. When taking into account the magnification of the imaging system, $m_{\text{sys}} \approx 2$, these points correspond nicely to the points around $z = 4$ mm in the simulation from chapter 3.

As a suitable profile was identified, it was evaluated using the fill-factor Γ and the modulation M as introduced in chapter 3. Fig. 8.10(a) shows the measured total intensity distribution from the array at $z = 16$ mm, whereas for comparison, Fig. 8.10(b) shows the corresponding profile from the simulation.

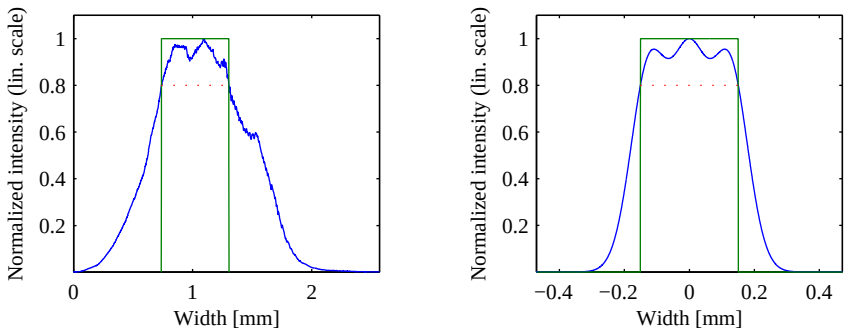

(a) Measured profile at $z = 16$ mm

(b) Simulated profile at $z = 4$ mm

Figure 8.10: Comparison between the measured intensity profile and the corresponding simulation result. Due to the poor performance of the right fibre, the fill factor was only 55 % for the measurement, compared to 78 % for the simulation. A threshold value of $0.8 I_{\max}$ was used in both cases.

However, the single laser performance has to be taken into account when quantifying the results. The fill-factor for the measured beam is 55 %, compared to 78 % for the simulation. The low value is due to the low peak intensity of the fibre to the right in Fig. 8.10(a), since for calulating Γ, the intensity profile is essentially truncated where the intenstiy drops below the threshold value. Evidently, the informative value of the fill-factor decreases as the individual lasers perform more differently. For both distributions, a threshold of $0.8 I_{\max}$ was used.

Damage and Component Lifetime

The reliability and long-term stability of the array is of great importance for any application. A high component lifetime is therefore substantial and a major concern. During the experiments, problems became apparent with the durability of the pump diodes and the gain fibres.

One pump diode failed, most likely because of a voltage spike in the power supply. The diodes were current-controlled with a laser driver (Opto Power Corporation, OPC-PS 4005), because due to their characteristic U-I-curve, even a very small increase in driving voltage, can lead to an increase in driving current, which is well above the damage threshold of the diode. The failure most likely occurred when a high-voltage device was unplugged from the same power line to which the laser driver was connected. It thereby created a high-voltage spike, which led to current-induced thermal damage in the semiconductor crystal.

Measurements showed a drastic decrease in optical output power after the breakdown (Fig. 8.11(a), compare with Fig. 4.3), as well as a broadened and shifted output spectrum (Fig. 8.11(b)). This suggests that the end-faces of the semiconductor were broken so that no laser operation could built up anymore.

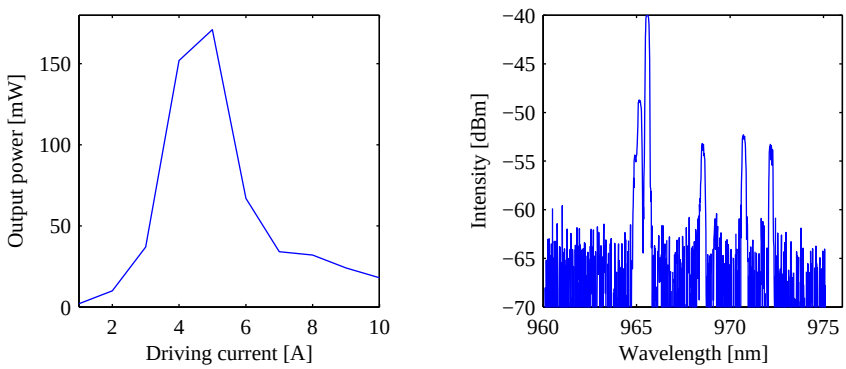

(a) Output power (b) Spectrum

Figure 8.11: Performance of the broken pump diode LD2. It shows a greatly reduced output power as well as a broadened and shifted output spectrum.

Another cause of failure could be back-coupled laser light. Once the light is coupled back into the pump fibre, it would be guided to the semiconductor chip and would generate additional heating on its crystal surface. To prevent this, a low-pass filter was used (mirror M1 in Fig. 8.1) which transmits light at the pump wavelength, whereas it is highly reflective at the laser wavelength. However, even though the reflectivity at the laser wavelength is close to 100 %, it cannot be

guaranteed that a fraction of the laser light during self-pulsed operation might not cause some damage of the semiconductor.

Besides the pump diodes, two fibre ends broke during operation. The damage for both fibres occurred on the side of the output coupler, where the fibre-ends were cleaved. Thermal effects are more prominent on this side, since the pump and the laser intensity is higher at the output-coupler. The broken fibre ends (damage on fibres 1 and 2) are shown in Fig. 8.12.

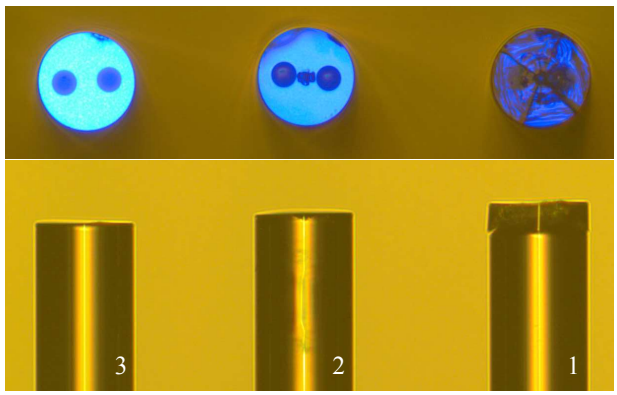

Figure 8.12: Broken fibre ends (fibres 1 and 2). The damage occurred on the output-coupling end with the cleaved end-faces.

Fibre 1 showed two perpendicular cracks through the centre of the fibre. The damaged region extended approximately 30 µm from the front-face into the fibre, which suggests that high stress was created in the silica glass, possibly due to absorption in a hot-spot. Fibre 2 showed damage only on the surface of the fibre, in the vicinity of its core. This was believed to be due to poor cleaving of the fibre or a polluted surface. Poor cleaving was supported by the M^2-measurement, which revealed a low beam quality of fibre 2. Pollution could have come from settled debris from the lab.

Another possible cause of damage was self-pulsing. As described in section 8.1, all fibres had a purely pulsed output. Even though the observed pulses (peak power of approx. 10 MW/cm^2) did not reach the damage threshold of Yb-doped silica glass of around 500 MW/cm^2 [26], stronger temporal instabilities are known to cause substantial fibre damage [27].

To increase the durability of the system, measures have to be taken. Protection from voltage spikes can for instance be obtained, by adding a low-pass filter to the power supply. Self-pulsing, on the other hand, can be suppressed by stronger pumping or by increasing the cavity photon lifetime, e. g. by increasing the cavity length with a passive fibre [22, 24].

Chapter 9

Nonlinear Frequency Conversion

Many array-applications require light of higher frequencies e. g. visible light for displays or UV light for laser writing. An efficient conversion process requires a light source of narrow linewidth and with linearly polarized output. This is why considerable effort was put into achieving a high polarization extinction ratio (chapter 6) and a frequency-locked spectrum using a volume Bragg grating (chapter 7).

A preliminary experiment was performed, using only fibre 2, to show that the laser setup can be used for nonlinear frequency conversion.

9.1 Second Harmonic Generation

Light of the second harmonic at $\lambda_{\mathrm{SHG}} = 515$ nm was generated with a crystal of periodically poled potassium titanyl phosphate (PPKTP) in a setup according to Fig. 9.1. The setup was placed approximately 1.5 m from the laser, which delivered approximately 3.6 W at 1030 nm. Two metallic mirrors were used to aim the collimated beam on the crystal. The nonlinear material had a poling period of 7.99 µm and the length of the poled region was 8 mm. The effective nonlinear coefficient is approximately $d_{\mathrm{eff}} = 2d_{33}/\pi = 10.8$ pm/V [28], where a d_{33}-coefficient of 16.9 pm/V (at 1064 nm) was assumed [29].

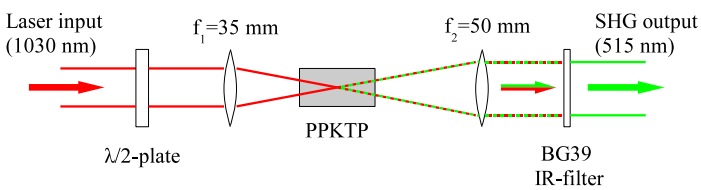

Figure 9.1: Setup for second harmonic generation with PPKTP.

The polarization direction of the collimated laser light was first rotated with a $\lambda/2$-plate to be along the c-direction of the nonlinear crystal. This direction utilizes the nonlinear susceptibility coefficient d_{33} for the conversion process, which is the highest coefficient in KTP [30].

The focussing lens was chosen for optimal conversion efficiency according to Boyd-Kleinman theory [31], taking into account the beam's M^2-factor. In a periodically poled crystal with no walk-off, the optimal focussing parameter is $\xi_\mathrm{m} = l/b = 2.84$, where l and b are the crystal length and the confocal parameter, respectively. For a crystal length of 8 mm, this requires a focal spot diameter inside the nonlinear material of approximately 30 µm. Using the data from the measurement of the M^2-factor from section 8.1, it was found that the optimal focal spot size was obtained by focussing with a lens of 35 mm focal length.

The phase-matching conditions of the PPKTP crystal change with temperature due the thermo-optic effect and thermal expansion. The crystal was designed to be most efficient at 80 °C, therefore the crystal was heated up on a temperature-controlled plate.

The output from the PPKTP crystal was collimated with a 50 mm lens and a dichroic mirror as well as a BG39 filter was used to remove the remaining infrared light. Using this setup, the maximum output power of the second harmonic was measured to be approximately 190 mW. Taking into account the Fresnel losses at both end-faces of the crystal, the internal efficiency of the second harmonic process is given by:

$$\eta_\mathrm{SHG} = \frac{P_{2\omega}}{P_\omega} = \frac{0.21\ \mathrm{W}}{3.3\ \mathrm{W}} = 6.4\,\%, \tag{9.1}$$

where P_ω and $P_{2\omega}$ are the average power of the fundamental and the second harmonic, respectively. Both values, P_ω and $P_{2\omega}$, denote powers inside of the crystal.

The conversion efficiency of a nonlinear process depends on the peak intensity of the fundamental beam, rather than on its average power. Therefore, the self-pulsed behaviour of the fibre laser was beneficial in this experiment. The duty cycle of the output was approximately 15 %, giving an average peak power of the fundamental beam inside the crystal of around 22 W. Using this quantity, rather than the average power, the normalized conversion efficiency of the SHG process is given by: $\eta_\mathrm{SHG,norm} = 0.4\,\%\ (\mathrm{W\ cm})^{-1}$, where a duty-cycle for the second harmonic of 15 % was assumed.

The experiments showed that light of reasonable power at 515 nm could be generated. The laser setup is therefore a viable source for second harmonic generation. Considering the preliminary nature of the experiments, the conversion efficiency can most likely further be increased, e. g. by a more accurate choice of the focussing lens and a better control of other parameters, such as the temperature of the PPKTP crystal.

9.2 Sum Frequency Generation

Light of the second harmonic, together with the remaining light of the fundamental frequency, was in a following experiment used to produce light of the third harmonic at $\lambda_{\mathrm{SFG}} = 343$ nm. This was achieved by sum frequency generation (SFG) using a lithium triborate (LBO) crystal. The principal setup is shown in Fig. 9.2.

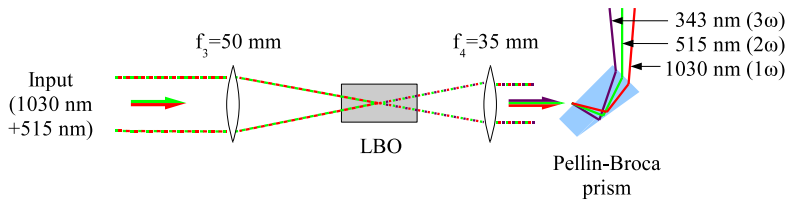

Figure 9.2: Setup for sum frequency generation with LBO.

The LBO crystal was cut for type-I phase-matching ($\theta = 90°$, $\phi = 40.1°$) and had an effective nonlinear coefficient of $d_{\mathrm{eff}} = 0.69$ pm/V. The walk-off angle was $\rho = 18.72$ mrad, yielding a walk-off parameter of $B = 8.33$ for the second harmonic wave and hence, an optimal focussing parameter of $\xi_m = 1.39$ [31]. Accordingly, the optimal focal spot diameter is around 40 µm, which was approximately achieved by focussing with a lens of 50 mm focal length.

The emitted light was collimated with a fused silica lens of focal length 35 mm. Thereafter, the three wavelengths were separated by a dispersive Pellin-Broca prism.

All three wavelengths were aimed on a paper screen from which the fluorescence of the UV light could clearly be seen. After the light of the fundamental and second harmonic were filtered out by a UG1-filter (Schott), the intensity of the third harmonic was measured to be approximately 0.05 mW, which was close to the detection limit the the power meter.

The experiment showed that UV-light could be generated using SFG. However, due to an unoptimized setup, the conversion efficiency was low. A more careful selection of the focussing lens for the input beams, better control of the spatial overlap of the fundamental and the second harmonic, as well as an optimized crystal length would most likely increase the UV output considerably.

Chapter 10

Conclusions

I have designed and built an array of parallel, Yb-doped fibre lasers, operating at 1 µm, for use as a line-source in laser writing and display applications. For a line-beam, parallel stacking of fibre lasers presents a very convenient way to scale the power of the source. This particular beam profile has relaxed constraints on beam quality in one dimension, which makes the array-approach very promising.

The array was built with free-space pumping and operating of three parallel fibre lasers, where the same optics were used simultaneously for all fibres. This approach ensures high flexibility in terms of replacing and adding components, while at the same time, the number of optical elements is greatly reduced. The setup allowed for efficient operation of three parallel fibre lasers. The optical-to-optical efficiency of the individual lasers was between 40 % and 50 %, with optical output powers between 2.5 W and 3.3 W, yielding a total output power of the array of 9 W.

A requirement for both laser writing and display applications, is the possibility of nonlinear frequency conversion, to generate wavelengths in the visible and the ultraviolet spectral regions. Therefore, the array was designed such that a linearly polarized and spectrally narrow output was obtained. The achieved polarization extinction ratios (PER) between two perpendicular polarization directions of the individual output beams were between 13 dB and 23 dB. The wavelengths were locked at 1029 nm using a volume Bragg grating and had spectral full widths at half maximum of below 0.1 nm. This allowed for efficient frequency conversion, where 190 mW of green and approximately 0.05 mW of ultraviolet light were generated using a single fibre laser.

A simulation programme was written to understand the behaviour of the system and to verify the working principle of the setup. The programme simulates the intensity distribution of the output from an array of an arbitrary number of equally spaced, parallel fibre lasers. Measurements of the beam profile from the array showed good agreement with the simulation. It was shown that a nearly homogeneous intensity distribution can be generated, which can be shaped into a

line-beam with an approximate top-hat profile.

The optical output power of the array scaled linearly with the number of fibres. Hence, this setup provides a good means to increase the laser output for systems in which the constraints on beam quality in one direction are relaxed.

10.1 Outlook and Future Work

The alignment of optics and fibres was achieved with sufficient accuracy for three lasers. However, extending this setup to a larger number of fibres will at some point be limited due to off-axis aberrations, since only single lenses were used for imaging of all fibres. To some extend, the accuracy can be increased, e. g. by using highly precise etched silica V-grooves for positioning of the fibres (e. g. from OZ Optics Ltd. [32]) and closer stacking. However, when using more than 7 to 9 fibres, alternative approaches might be preferable.

To increase the conversion efficiency of the nonlinear processes, the PER of the individual lasers can be further increased. This could be achieved, e. g. by aligning the fibres according to their axis of birefringence, rather than according to their geometric structure. In-situ monitoring of the PER as the fibre is being aligned, is one way to achieve improvement. The optical inspection method as used in this thesis is fundamentally imperfect and lacks of high accuracy.

Component lifetime was a major concern during the thesis. Two broken pump lasers as well as two damaged fibre ends raise the question of durability of the setup. Longer lifetime could possibly be achieved by the suppression of self-pulsing e. g. by increasing the pump power. Increasing the individual laser power has the additional advantage of increasing the efficiency of the nonlinear conversion process. Moreover, a higher surface quality of the fibre end-faces and protection against debris would increase the damage threshold and the durability of the setup as well.

Improving the surface quality of the end-faces is also expected to lower the M^2-factor of the beams. With appropriate out-coupling optics, the setup should approach $M^2 \approx 1$ rather easily. Bending the fibres is a means to suppress higher order modes, which is a further requirement for a good beam quality.

Using the design approach as presented in this thesis and based on commercially available lasers with individual output powers of 150 W [33], arrays with total output powers of 1 to 1.5 kW are expected to be contrivable.

References

[1] M. Sheikh and L. Li, *Understanding the effect of non-conventional laser beam geometry on material processing by finite-element modelling*, Proceedings of the Institution of Mechanical Engineers, Part C: Journal of Mechanical Engineering Science **224**, 1061 (2010).

[2] S. Kou, D. Sun and Y. Le, *A fundamental study of laser transformation hardening*, Metallurgical and Materials Transactions A **14**, 643 (1983).

[3] S. Hell and J. Wichmann, *Breaking the diffraction resolution limit by stimulated emission: stimulated-emission-depletion fluorescence microscopy*, Optics Letters **19**, 780 (1994).

[4] M. Oka, K. Kimura, Y. Maeda, K. Takahashi, N. Iwase and H. Tamada, in *A new compact continuous-wave green laser with line beam*, , edited by P. E. Powers (SPIE, 2008), No. 1, 68750L.

[5] Y. Qi, S. Chu, Y. Bi, M. Zhou, W. Yan, Y. Zhang, Y. Wang, B. Yan, B. Wang, T. Wu, C. Feng, Y. Liu, T. Fang and G. Zheng, *A compact continuous-wave green laser with line beam for laser projection*, Optics and Lasers in Engineering **48**, 737 (2010).

[6] N. Kramer, M. Niesten and C. Schönenberger, *Resistless high resolution optical lithography on silicon*, Applied Physics Letters **67**, 2989 (1995).

[7] MicroChemicals GmbH, *Application Notes: Exposure of Photoresists*, http://www.microchemicals.com/technical_information/exposure_photoresist.pdf (August 19 2010).

[8] M. J. F. Digonnet, *Rare-Earth-Doped Fiber Lasers and Amplifiers* (CRC Press, Boca Raton, FL, 2001).

[9] P. Jelger, P. Wang, J. K. Sahu, F. Laurell and W. A. Clarkson, *High-power linearly-polarized operation of a cladding-pumped Yb fibre laser using a volume Bragg grating for wavelength selection*, Opt. Express **16**, 9507 (2008).

[10] C. Liu, A. Galvanauskas, V. Khitrov, B. Samson, U. Manyam, K. Tankala, D. Machewirth and S. Heinemann, *High-power single-polarization and single-transverse-mode fiber laser with an all-fiber cavity and fiber-grating stabilized spectrum*, Optics letters **31**, 17 (2006).

[11] D. Xue, A. El-Damak and X. Gu, *All-fiber single polarized Yb-doped fiber laser with a high extinction ratio*, Optics Communications (2009).

[12] A. Shirakawa, M. Kamijo, J. Ota, K. Ueda, K. Mizuuchi, H. Furuya and K. Yamamoto, *Characteristics of Linearly Polarized Yb-Doped Fiber Laser in an All-Fiber Configuration*, IEEE Photonics Technology Letters **19**, 1664 (2007).

[13] V. Paramonov, A. Kurkov, O. Medvedkov and V. Tsvetkov, *Single-polarization cladding-pumped Yb-doped fiber laser*, Laser Physics Letters **4**, 740 (2007).

[14] O. Svelto, *Principles of lasers* (Plenum press, 1998).

[15] A. Yariv, *Quantum Electronics* (Wiley, New York, 1989).

[16] G. Agrawal, *Nonlinear Fiber Optics*, 4 ed. (Academic Press, 2007).

[17] B. E. A. Saleh and M. C. Teich, *Fundamentals of Photonics* (Wiley, New York, 1991).

[18] D. Marcuse, *Loss Analysis of Single-Mode Fiber Splices*, The Bell System Technical Journal **56**, 703 (1977).

[19] H. Pask, R. Carman, D. Hanna, A. Tropper, C. Mackechnie, P. Barber and J. Dawes, *Ytterbium-Doped Silica Fiber Lasers: Versatile Sources for the 1-1.2 μm Region*, IEEE Journal of Selected Topics in Quantum Electronics **1**, 2 (1995).

[20] K. Uehara and H. Kikuchi, *Transmission of a Gaussian beam through a circular aperture*, Appl. Opt. **25**, 4514 (1986).

[21] F. Brunet, Y. Taillon, P. Galarneau and S. LaRochelle, *A Simple Model Describing Both Self-Mode Locking and Sustained Self-Pulsing in Ytterbium-Doped Ring Fiber Lasers*, J. Lightwave Technol. **23**, 2131 (2005).

[22] W. Guan and J. R. Marciante, *Complete elimination of self-pulsations in dual-clad ytterbium-doped fiber lasers at all pumping levels*, Opt. Lett. **34**, 815 (2009).

[23] R. G. Smith, *Optical Power Handling Capacity of Low Loss Optical Fibers as Determined by Stimulated Raman and Brillouin Scattering*, Appl. Opt. **11**, 2489 (1972).

[24] B. Upadhyaya, A. Kuruvilla, U. Chakravarty, M. Shenoy, K. Thyagarajan and S. Oak, *Effect of laser linewidth and fiber length on self-pulsing dynamics and output stabilization of single-mode Yb-doped double-clad fiber laser*, Appl. Opt. **49**, 2316 (2010).

[25] J. E. Hellstrom, B. Jacobsson, V. Pasiskevicius and F. Laurell, *Finite beams in reflective volume Bragg gratings: Theory and experiments*, IEEE JOURNAL OF QUANTUM ELECTRONICS **44**, 81 (2008).

[26] A. Carter, B. Samson, K. Tankala, D. Machewirth, V. Khitrov, U. Manyam, F. Gonthier and F. Seguin, *Damage mechanisms in components for fiber lasers and amplifiers*, SPIE (2005), Vol. 5647, 561–571.

[27] A. Smith and B. Do, *Bulk and surface laser damage of silica by picosecond and nanosecond pulses at 1064 nm*, Applied Optics **47**, 4812 (2008).

[28] S. Wang, *Fabrication and characterization of periodically poled KTB and RB-doped KTB for applications in the visible and UV*, Ph.D. thesis, KTH, Physics, 2005.

[29] H. Vanherzeele and J. Bierlein, *Magnitude of the nonlinear-optical coefficients of $KTiOPO_4$*, Optics Letters **17**, 982 (1992).

[30] J. D. Bierlein and H. Vanherzeele, *Potassium titanyl phosphate: properties and new applications*, J. Opt. Soc. Am. B **6**, 622 (1989).

[31] Y. Chen and Y. Chen, *Analytical functions for the optimization of second-harmonic generation and parametric generation by focused Gaussian beams*, Applied Physics B: Lasers and Optics **76**, 645 (2003).

[32] OZ Optics Ltd., http://www.ozoptics.com/ALLNEW_PDF/DTS0077.pdf (August 14 2010).

[33] IPG Photonics Corp., http://www.ipgphotonics.com/products_1micron_lasers_singlefrequency_ylr-lp-sfs.htm (August 17 2010).